Article

Developmental Cell

A Mechanosensitive RhoA Pathway that Protects Epithelia against Acute Tensile Stress

Graphical Abstract

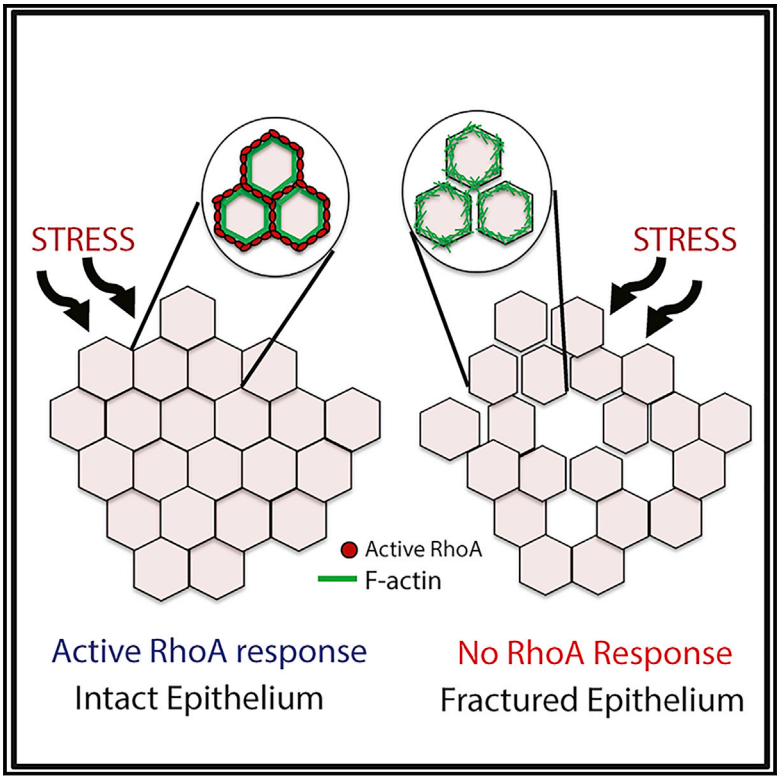

Authors

Bipul R. Acharya, Alexander Nestor-Bergmann, Xuan Liang, ..., Oliver E. Jensen, Zev Bryant, Alpha S. Yap

Correspondence

a.yap@uq.edu.au

In Brief

Acharya et al. report a mechanotransduction pathway that activates RhoA at adherens junctions when mechanical stress is applied to epithelial monolayers. RhoA signaling is elicited downstream of the mechanosensitive actin-based motor, Myosin VI, and stimulates junctional actin assembly via mDia1 to protect epithelial integrity.

Highlights

- Acute tensile stress on epithelial monolayer activates RhoA at adherens junctions
- Myosin VI is a force sensor responsible for activating RhoA
- RhoA signals to stimulate mDia1-mediated F-actin assembly at junctions
- Mechanotransduction reinforces the tensile strength of multicellular vertices

Acharya et al., 2018, Developmental Cell *47*, 439–452
November 19, 2018
https://doi.org/10.1016/j.devcel.2018.09.016

CellPress

Developmental Cell
Article

A Mechanosensitive RhoA Pathway that Protects Epithelia against Acute Tensile Stress

Bipul R. Acharya,[1] Alexander Nestor-Bergmann,[2,7] Xuan Liang,[1,7] Shafali Gupta,[1] Kinga Duszyc,[1] Estelle Gauquelin,[3] Guillermo A. Gomez,[1,8] Srikanth Budnar,[1] Philippe Marcq,[4] Oliver E. Jensen,[5] Zev Bryant,[6] and Alpha S. Yap[1,9,*]
[1]Division of Cell Biology and Molecular Medicine, Institute for Molecular Bioscience, The University of Queensland, St. Lucia, Brisbane, QLD 4072, Australia
[2]Department of Physiology, Development and Neuroscience, University of Cambridge, Cambridge CB2 3DY, UK
[3]Institut Jacques Monod, CNRS, UMR 7592, Universite Paris Diderot, Sorbonne Paris Cité, Paris 75205, France
[4]Physico Chimie Curie, Institut Curie, Sorbonne Universite, PSL Research University, Paris and CNRS UMR 168, Paris 75005, France
[5]School of Mathematics, University of Manchester, Manchester M13 9PL, UK
[6]Department of Bioengineering, Stanford University and Department of Structural Biology, Stanford University School of Medicine, Stanford, CA 94305, USA
[7]These authors contributed equally
[8]Present address: Centre for Cancer Biology, SA Pathology and the University of South Australia, Adelaide, SA, Australia
[9]Lead Contact
*Correspondence: a.yap@uq.edu.au
https://doi.org/10.1016/j.devcel.2018.09.016

SUMMARY

Adherens junctions are tensile structures that couple epithelial cells together. Junctional tension can arise from cell-intrinsic application of contractility or from the cell-extrinsic forces of tissue movement. Here, we report a mechanosensitive signaling pathway that activates RhoA at adherens junctions to preserve epithelial integrity in response to acute tensile stress. We identify Myosin VI as the force sensor, whose association with E-cadherin is enhanced when junctional tension is increased by mechanical monolayer stress. Myosin VI promotes recruitment of the heterotrimeric Gα12 protein to E-cadherin, where it signals for p114 RhoGEF to activate RhoA. Despite its potential to stimulate junctional actomyosin and further increase contractility, tension-activated RhoA signaling is necessary to preserve epithelial integrity. This is explained by an increase in tensile strength, especially at the multicellular vertices of junctions, that is due to mDia1-mediated actin assembly.

INTRODUCTION

Epithelia are the fundamental tissue barriers of the body. Epithelial integrity requires that cells be coupled together by specialized cell-cell junctions that can resist mechanical stresses applied to tissues. Of these junctions, a notable role is played by cadherin-based adherens junctions (AJs), which bear mechanical tension and preserve tissue integrity (Harris et al., 2014; Levine et al., 1994). This tension arises both from intrinsic forces, where the contractile actomyosin cytoskeleton is coupled to cadherin adhesion, and extrinsic forces such as those associated with animal locomotion and gut peristalsis (Charras and Yap, 2018). Intrinsic junctional tension is evident even in apparently quiescent monolayers (Choi et al., 2016; Ratheesh et al., 2012); but tension is also stimulated to mediate a wide range of morphogenetic processes, from cell-cell rearrangements (Lecuit and Lenne, 2007) to cell extrusion (Saw et al., 2017; Michael et al., 2016). Thus, increases in junctional tension often serve fundamental physiological roles. In all these circumstances, however, it is necessary for cell-cell cohesion to be preserved despite the application of force.

One potential solution to this challenge is for cells to possess mechanisms that can sense when tensile stresses are applied on AJs and elicit proportionate homeostatic responses that preserve tissue integrity. Indeed, it is increasingly evident that mechanosensitive molecular mechanisms exist at AJs (le Duc et al., 2010; Yonemura et al., 2010), and a wide range of cell signals are found there that can modulate adhesion and the cytoskeleton, key elements for junctional integrity (Yap et al., 2018; Pruitt et al., 2014). For example, catch bonds mediate adhesive binding of cadherin ectodomains (Manibog et al., 2014) as well as interactions between the cadherin molecular complex and actin filaments (Buckley et al., 2014), while Rho family GTPases and Src family kinases are found to signal at junctions (Gomez et al., 2015; Ratheesh et al., 2012). Despite this growing wealth of candidates, we have yet to holistically characterize a pathway that might maintain junctional integrity against mechanical stress. For this, we would need to identify key mechanosensitive receptors, the signaling pathways that are elicited, and the effector mechanisms that preserve epithelial integrity.

We now report such a pathway that preserves epithelial integrity against both intrinsically generated and externally applied tensile stress. We show that junctional RhoA signaling is activated in response to mechanical stress. We identify the mechanosensitive Myosin VI as a key force sensor that interacts with E-cadherin to promote recruitment of the RhoA activators,

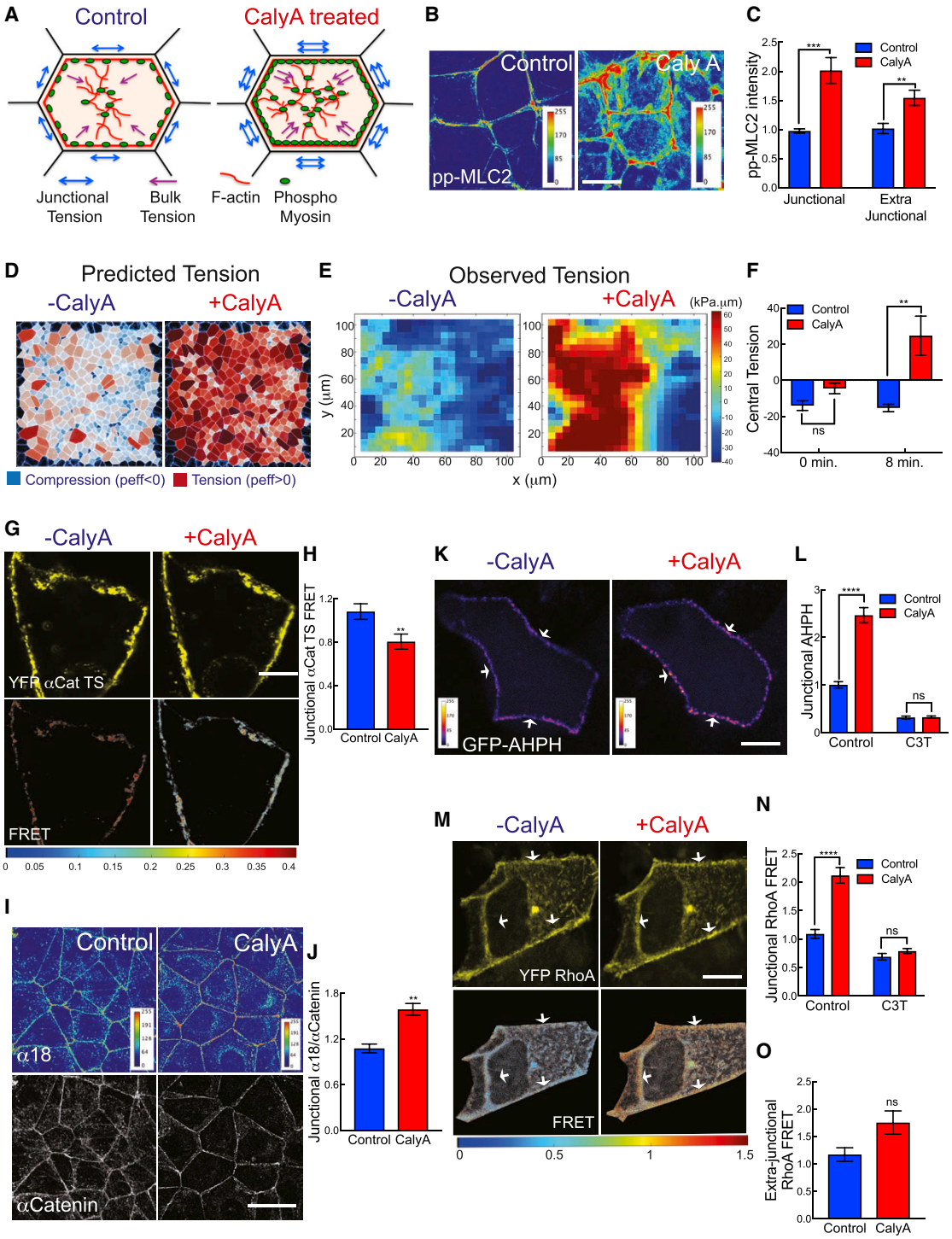

Figure 1. Tensile Monolayer Stress Activates RhoA at the Zonula Adherens

(A) Cartoon of contractile activation by calyculin A. Unless otherwise indicated, calyculin was added for 12 min.

(B and C) Calyculin A increases active Myosin II (ppMLC2, pT18/S19) at junctions and in the extrajunctional compartment: representative images (B) and quantitation (C).

(D) Distribution of effective cell-level pressures, P^{eff}, predicted by the vertex model before (Left; $\phi_A = 1$, $\phi_P = 1$) and after (Right; $\phi_A = 0.75$, $\phi_P = 1.25$) bulk and cortical contractility were increased to mimic calyculin (ϕ_A and ϕ_P represent fractional change in preferred area and cortical stiffness, respectively; see Computational Supplement, Data S1). Red marks cells predicted to be under tension ($P^{eff} > 0$); blue denotes net compression ($P^{eff} < 0$).

(E and F) Calyculin A increases tissue-level tension obtained by Bayesian inversion stress microscopy. (E) Representative spatial maps before (−CalyA) and after (+CalyA, 8 min) calyculin A, taken away from the boundaries of the domain chosen for traction force measurement. (F) Quantitation of average central tension (kPa.μm; n = 3 independent measurements); control is buffer alone.

(legend continued on next page)

Gα12 and p114 Rho guanine nucleotide exchange factor (GEF). Surprisingly, despite increasing junctional actomyosin, this pathway prevents epithelial junctions from fracturing upon application of tension. Combining a predictive mechanical model for epithelial junctions with experiments, we find that this can be explained by an increase in tensile strength due to mDia1-dependent stabilization of E-cadherin at multicellular vertices.

RESULTS

Mechanical Tension Activates RhoA at AJs

We first combined computational predictions and experiments to understand how increasing contractility might affect monolayers. Intrinsic contractile stress was increased by treating confluent Caco-2 monolayers with calyculin A (henceforth calyculin; 20 nM, for 8–30 min; Figure 1A) which stimulates non-muscle myosin (NMII) and regulates its turnover by inhibiting the PP2A subunit of myosin phosphatase (Giannone et al., 2007; Vallotton et al., 2004). Western analysis confirmed that phosphorylation of myosin regulatory light chain (Thr18/Ser19; ppMLC) was increased, an effect that was largely blocked by prior addition of the ROCK inhibitor Y-27632 (Figures S1A and S1B); and immunofluorescence microscopy showed that ppMLC was increased both at junctions and at extrajunctional regions (Figures 1B and 1C).

We then adopted a commonly used, vertex-based model of an epithelial tissue to predict how these changes in cell contractility might affect cell- and tissue-level stress (Nestor-Bergmann et al., 2018a; Fletcher et al., 2014; Farhadifar et al., 2007; Nagai and Honda, 2001; Honda and Eguchi, 1980). Starting with segmented images of a confluent monolayer, we computationally introduced additional contractility in the bulk and cortex of the cell, consistent with the sites where ppMLC was increased. The model was then used to infer the consequent patterns of cell-level mechanical stress, identifying cells that are under relative net tension or compression (see Equation 7 of the Computational Supplement, Data S1). This predicted that the proportion of cells under net tension increases following treatment with calyculin (Figure 1D and Video S1). For a monolayer with boundary conditions that constrain its size, as might be expected of confluent epithelial monolayers, global isotropic tissue stress increases but with very little movement in the tissue.

To test these predictions, we first examined the morphological response of monolayers using endogenous E-cadherin that was CRISPR-Cas9-engineered to bear a GFP tag at its C terminus (Liang et al., 2017). Consistent with the model, despite subtle shape changes, the cells did not translocate, and the junctions remained intact for ~12 min, until they fractured at the very end of the videos (Video S1). Then we measured global patterns of force with traction force microscopy (TFM) and applied Bayesian inversion stress microscopy (BISM) to the TFM data to infer the tissue-level patterns of mechanical stress (Saw et al., 2017; Nier et al., 2016). Calyculin increased both the traction forces applied to the substrate (Figure S1C) and the tension within the monolayer (Figures 1E and 1F), as predicted by the model.

Finally, we asked if this coarse-grained increase in tissue tension led to changes in tension at AJs. As reported earlier (Acharya et al., 2017), calyculin increases AJ tension measured by recoil velocity after laser ablation, and this effect was blocked by Y-27632 (Figure S1D). We further confirmed this at the molecular level using a fluorescence resonance energy transfer (FRET)-based tension sensor incorporated into α-catenin (αCat-TS) (Acharya et al., 2017). Calyculin decreased energy transfer across αCat-TS (Figures 1G and 1H), consistent with an increase in tension. This was supported by increased staining for the tension-sensitive α-18 epitope of α-catenin (Figures 1I and 1J) (Yonemura et al., 2010). Thus, increased tissue tension was associated with an increase in tension at AJs.

We then used a location biosensor for active GTP-RhoA (AHPH, derived from the C terminus of anillin [Piekny and Glotzer, 2008]) to monitor the response of RhoA signaling to calyculin. As previously reported (Priya et al., 2015; Ratheesh et al., 2012), active RhoA signaling in established steady-state epithelial monolayers was consistently found in a prominent zone at the zonula adherens (ZA) and variably in the medial-apical cortex (Figures 1K and S1E). The intensity of the junctional signal increased rapidly with calyculin (Figures 1K and 1L; Video S2). This was supported with a FRET-based RhoA activity sensor that showed increased energy exchange principally at junctions on addition of calyculin (Figures 1M–1O). Inhibition with C3-transferase confirmed that these responses were specific (C3-T; Figures 1L and 1N). By contrast, little change in GTP-RhoA was evident at cell-substrate interfaces (Figures S1F and S1G). Together, these findings suggested that contractile tension stimulates junctional RhoA signaling.

To reinforce this conclusion, we adopted the complementary approach of growing Caco-2 cells on flexible substrata and then subjecting them to an acute equibiaxial stretch (10%, 10 min; Figure S1H). Stretch increases the proportion of cells under net tension within a tissue (Nestor-Bergmann et al., 2018a; Nestor-Bergmann et al., 2018c; Wyatt et al., 2015), and we confirmed that tension on the cadherin complex increased with both αCat-TS and α-18 staining (Figures S1I–S1L). Again, we observed increased junctional RhoA signaling, measured both with AHPH (Figures S1M and S1N) and the RhoA-FRET sensor

(G and H) Calyculin A increases molecular-level tension across αE-Catenin, measured with a FRET-based αE-Cat tension sensor. Representative FRET images from a video (G) and FRET index quantitation by comparison between populations (H; normalized to untreated control).

(I and J) Tension-sensitive α18-mAb epitope immunofluorescence staining for αE-Catenin. Representative images (I) and quantitation (J; normalized to total junctional αE-Catenin).

(K and L) Calyculin A increases junctional AHPH: representative images from a video (K; arrows: cell-cell junctions; see Video S2) and quantitation by comparison between populations (normalized to cytosolic AHPH, L). C3-transferase (C3T) was a negative control.

(M–O) Effect of calyculin A on cellular RhoA-FRET. Representative images of FRET and YFP-RhoA signal from a video (M; arrows: cell-cell junctions) and quantitation by comparison between populations of FRET index at junctions (N) and in the extrajunctional compartment (O).

Data are means ± SEM; n = 3 independent experiments; see STAR Methods for details. ****p < 0.0001, ***p < 0.001, **p < 0.01; n.s., not significant; unpaired t test (H, J, and O) with Welch's correction or two-way ANOVA (C, F, L, and N) with Sidak's multiple comparisons test. Scale bars: 10 μm (B, G, K, and M) and 20 μm (I).

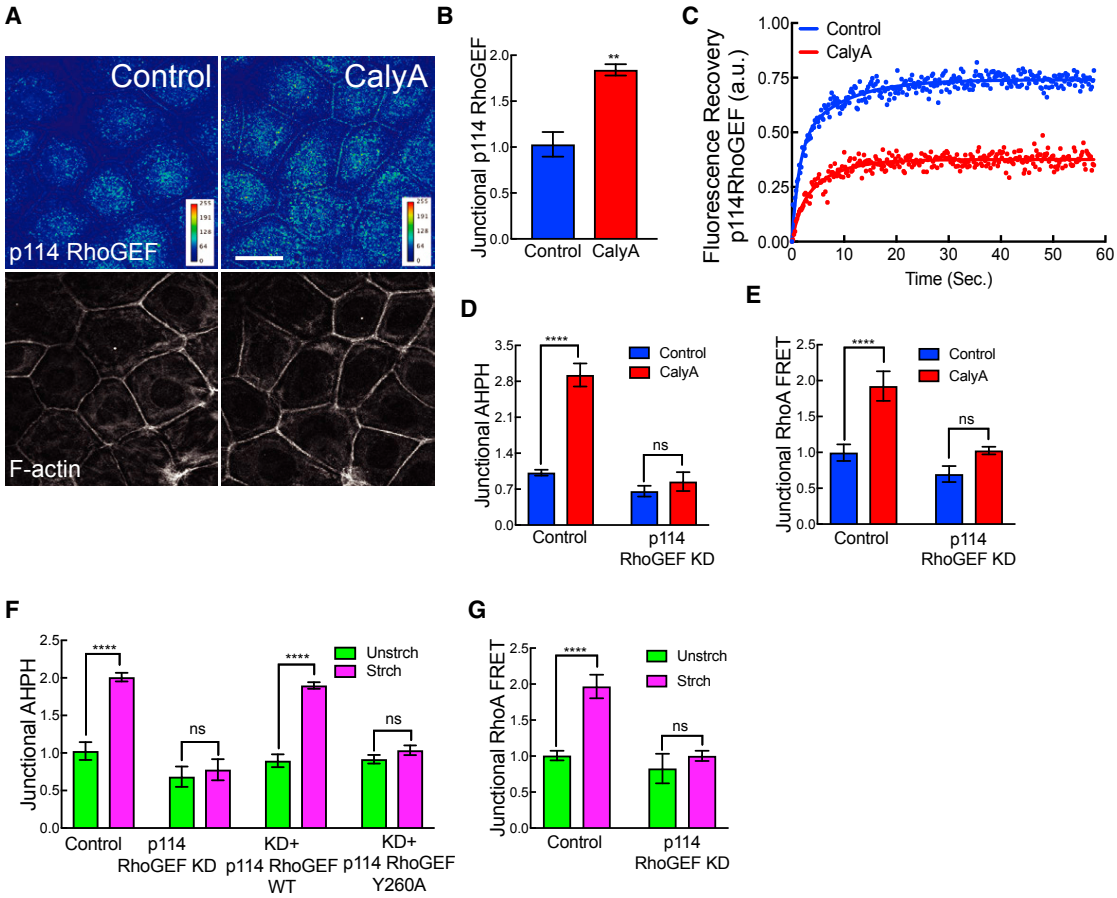

Figure 2. p114 RhoGEF Activates Junctional RhoA in Response to Tensile Stress

(A and B) Calyculin A increases p114 RhoGEF at junctions. Representative immunofluorescence images for p114 RhoGEF and F-actin (A) and quantitation of junctional fluorescence (B).

(C) Effect of calyculin A on FRAP of CFP-p114 RhoGEF^{WT} at junctions (data representative of 3 independent experiments).

(D and E) Effect of p114 RhoGEF KD on calyculin-stimulated RhoA signaling at the ZA measured by AHPH (D) and RhoA-FRET index (E).

(F) p114 RhoGEF KD inhibited stretch-induced activation of junctional RhoA, measured with AHPH. Effect of reconstitution with p114 RhoGEF^{WT} and p114 RhoGEF^{Y260A}.

(G) p114 RhoGEF KD inhibited stretch-induced junctional RhoA-FRET activity.

Data are means ± SEM; n = 3 independent experiments. ****$p < 0.0001$; n.s., not significant; unpaired t test (B) with Welch's correction or two-way ANOVA (D–G) with Sidak's multiple comparisons test. Scale bar: 20 μm.

(Figures S1P and S1Q), but no change at cell-substrate interfaces (Figure S1O). Together, we conclude that junctional RhoA responds to tensile monolayer stress. In order to dissect its functional significance, it was then necessary to define the molecular pathway by which tension activated RhoA.

p114 RhoGEF Mediates Tension-Activated RhoA Signaling

We first sought to identify the molecule(s) responsible for activating RhoA signaling in response to tensile stress. We screened candidate RhoA GEFs earlier implicated in mechanotransduction and/or junctional signaling (Figure S2A) (Lessey et al., 2012; Ratheesh et al., 2012; Guilluy et al., 2011; Terry et al., 2011). This led us to focus on p114 RhoGEF, whose junctional localization increased when mechanical stress was induced either with calyculin (Figures 2A and 2B) or stretch (Figures S2A and S2B). This was supported by fluorescence recovery after photobleaching (FRAP) studies, where CFP-p114 RhoGEF at junctions was stabilized by calyculin (Figure 2C and Table S1). In contrast, p115 RhoGEF and LARG did not localize to junctions in Caco-2 cells either before or after stretch (Figures S2A and S2B), although LARG increased in the extrajunctional pool; and while Ect2 and, to a minor extent, GEF H1 were found at the ZA, neither changed with tensile stimulation (Figures S2A and S2B).

We then depleted p114 RhoGEF by RNAi (knockdown [KD]) to test its role in tension-activated RhoA signaling (Figure S2C). p114 RhoGEF has been reported to support steady-state RhoA signaling at tight junctions (Terry et al., 2011). However, in our experiments, p114 RhoGEF KD did not significantly affect baseline levels of junctional AHPH at the ZA; instead, it abolished the increase stimulated either by calyculin (Figure 2D) or stretch (Figure 2F). This was confirmed by RhoA FRET (Figure 2E). In contrast, although steady-state junctional AHPH levels were decreased by Ect2 RNAi, the response to tensile stress was

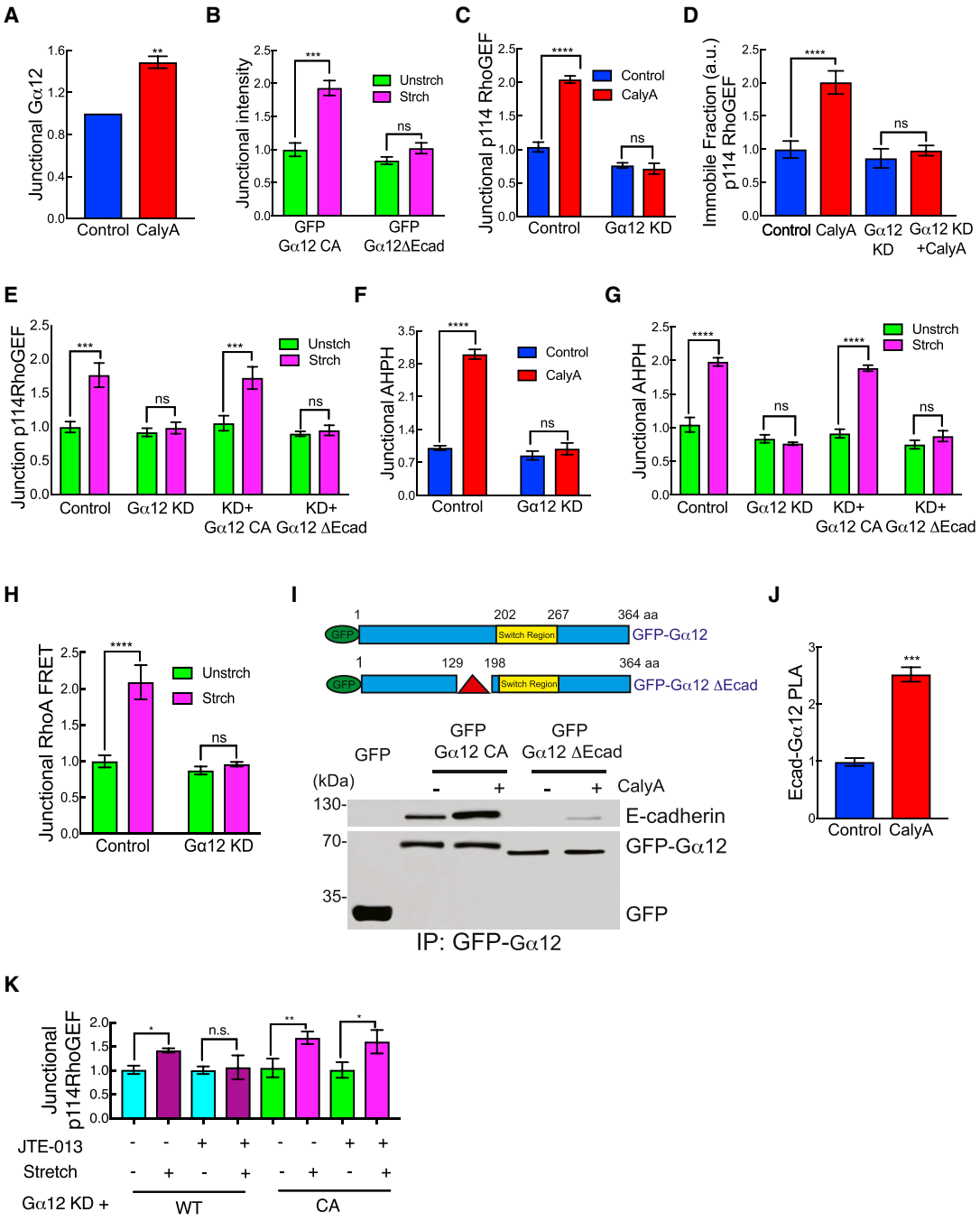

Figure 3. Role of Heterotrimeric Gα12 in Tension-Activated RhoA Signaling

(A) Effect of calyculin A on immunofluorescence intensity of junctional Gα12.

(B) Effect of mechanical stretch on junctional intensity of GFP- $G\alpha12^{CA}$ or GFP-$G\alpha12^{\Delta Ecad}$ reconstituted in Gα12 RNAi cells.

(C and D) Effect of Gα12 siRNA (KD) on junctional recruitment of p114 RhoGEF (C) and stabilization of junctional CFP-p114 RhoGEF (D; immobile fraction in FRAP normalized to controls) in response to calyculin A.

(E) Effect of Gα12 siRNA and reconstitution with GFP-$G\alpha12^{CA}$ or GFP-$G\alpha12^{\Delta Ecad}$ on junctional recruitment of p114 RhoGEF in response to mechanical stretch.

(F and G) Effect of Gα12 siRNA (F and G) and reconstitution with GFP-$G\alpha12^{CA}$ or GFP-$G\alpha12^{\Delta Ecad}$ (G) on tension-activated junctional RhoA signaling measured by AHPH in response to calyculin A (F) and mechanical stretch (G).

(H) Gα12 siRNA reduces junctional RhoA-FRET index response to mechanical stretch.

(I) Effect of calyculin on the E-cadherin-Gα12 interaction. Top: schematic representation of GFP-$G\alpha12^{CA}$ and GFP-$G\alpha12^{\Delta Ecad}$ constructs (Δ shows the deletion site in $G\alpha12^{\Delta Ecad}$). Bottom: GFP-$G\alpha12^{CA}$ or GFP-$G\alpha12^{\Delta Ecad}$ expressed in Gα12 KD cells were isolated by GFP-Trap and immunoblotted for E-cadherin and GFP before and after calyculin (representative of 3 independent experiments).

(legend continued on next page)

unaltered (Figure S2D). LARG or p115 RhoGEF KD had no effect on the baseline or stretch-stimulated levels of junctional AHPH (Figure S2D). This suggested a selective requirement for p114 RhoGEF to activate RhoA at the ZA in response to tension, whereas other GEFs, such as Ect2 (Ratheesh et al., 2012) mediated baseline signaling. The tension-activated RhoA response was restored to p114 RhoGEF KD cells by expression of an RNAi-resistant wild-type (WT)-p114 RhoGEF transgene (p114 RhoGEF^{WT}; Figures 2F and S2C), confirming the specificity of this effect. However, stretch-activated RhoA signaling was not restored by expression of a GEF-defective mutant (p114 RhoGEF^{Y260A}; Figures 2F and S2C). Together, these findings identified p114 RhoGEF as responsible for stimulating junctional RhoA signaling in response to tensile stress.

Gα12 Confers Junctional Specificity on p114 RhoGEF Recruitment

Then, we asked what was responsible for the selective junctional recruitment of p114 RhoGEF and subsequent RhoA activation. p114 RhoGEF is one of a number of GEFs that respond to heterotrimeric G-proteins of the Gα12/13 subclass (Martin et al., 2016; Siehler, 2009; Goulimari et al., 2005), which have also been implicated in cadherin-dependent morphogenesis (Kerridge et al., 2016; Lin et al., 2009) and can interact with the cadherin complex (Kaplan et al., 2001; Meigs et al., 2001). Indeed, Gα12 was faintly detectable at the ZA in unstressed monolayers but increased when tensile stress was applied, either with calyculin (Figures 3A and S3A) or extrinsic stretch (Figures 3B and S3B). In contrast, Gα13 was scarcely detectable at junctions in these cells at any stage (Figures S3D and S3E).

We further found that junctional recruitment of p114 RhoGEF by calyculin (Figure 3C) or stretch (Figure 3E) was impaired by Gα12 RNAi (Figure S3C). Stretch-induced recruitment of p114 RhoGEF was restored to Gα12 RNAi cells by expression of an RNAi-resistant constitutively active Gα12 transgene used to bypass any requirement for preactivation of Gα12 (Q231L; Gα12^{CA}; Figure 3E) (Krakstad et al., 2004). In contrast, stretch-induced recruitment of p114 RhoGEF was not affected by Gα13 KD (Figure S3G). This suggested that in Caco-2 cells, Gα12 was selectively responsible for recruiting p114 RhoGEF to junctions in response to tension. This was reinforced by FRAP experiments, which showed that calyculin did not stabilize CFP-p114 RhoGEF in Gα12 RNAi cells (Figures 3D and S3F; Table S1). Importantly, neither calyculin (Figure 3F) nor mechanical stretch (Figure 3G) increased junctional RhoA signaling when Gα12 was depleted, unlike Gα13 KD (Figure S3H). The specificity of this effect was established by rescue with Gα12^{CA} (Figure 3G). The RhoA FRET sensor confirmed that Gα12 was required for stretch to activate junctional RhoA (Figure 3H). Therefore, Gα12 was necessary for tensile stress to activate junctional RhoA signaling via p114 RhoGEF. As had been observed for p114 RhoGEF, Gα12 KD did not materially affect the baseline level of junctional RhoA activity but selectively perturbed the response to tensile stress (Figures 3F and 3G).

Earlier studies reported that Gα12 can bind directly to the C terminus of E-cadherin (Kaplan et al., 2001; Meigs et al., 2001). We therefore hypothesized that this interaction might confer junctional selectivity on the tension-activated RhoA response. To test this, we expressed GFP-Gα12^{CA} in Gα12 RNAi cells and isolated protein complexes with GFP-Trap (Figure 3I). E-cadherin associated with GFP-Gα12^{CA} at baseline, and the amount was substantially increased by calyculin (Figure 3I). This was supported by proximity ligation analysis (PLA), which showed an increased reaction between the two endogenous proteins at cell-cell junctions when tension was applied to monolayers (Figures 3J and S3I). We then sought to uncouple Gα12^{CA} from E-cadherin by deleting a 67-amino acid region that is separate from the switch region that activates p114 RhoGEF (Gα12$^{\Delta E\text{-cad}}$; Figure 3I; Meigs et al., 2005). Gα12$^{\Delta E\text{-cad}}$ behaved as a cadherin-uncoupled mutant: it did not co-immunoprecipitate with E-cadherin at baseline when expressed in Gα12 KD cells, and only a trace increase was seen after stimulation with calyculin (Figure 3I). Nor was Gα12$^{\Delta E\text{-cad}}$ recruited to junctions when monolayers were stretched (Figure 3B). Importantly, Gα12$^{\Delta E\text{-cad}}$ reconstituted in Gα12 KD cells did not support either the tension-sensitive junctional recruitment of p114 RhoGEF (Figure 3E) or the stretch-stimulated increase in junctional GTP-RhoA (Figure 3G). Together, these findings indicate that tensile stress activates RhoA signaling at the ZA by recruiting Gα12 to E-cadherin. Gα12 then represented a key intermediate that allowed force sensing at AJs to be transduced into chemical signaling by RhoA.

Gα-class proteins are typically activated in response to GPCR signaling, which makes them available for interaction with effectors (Oldham and Hamm, 2008). Indeed, E-cadherin was reported to preferentially bind GTP-Gα12 *in vitro* (Meigs et al., 2001). Therefore, we considered whether a GPCR might serve to generate an active pool of Gα12 that could be recruited to junctions. In a screen of GPCR inhibitors (Figure S3J), only JTE-013, a Sphingosine-1-phosphate receptor 2 ($S1P_2$) antagonist, blocked the stretch-induced recruitment of Gα12. To test whether $S1P_2$ might activate Gα12 for tension-activated RhoA signaling, we expressed either a WT Gα12 (Gα12^{WT}) or the constitutively-active Gα12^{CA} in Gα12 KD cells (Figure S3K) and measured the junctional recruitment of p114 RhoGEF in response to stretch as the immediate downstream target of Gα12 (Figure 3K). We predicted that if $S1P_2$ signaling was necessary for Gα12 to participate in this mechanotransduction pathway, then the recruitment of p114 RhoGEF would be inhibited by JTE-013 in the presence of Gα12^{WT} but not Gα12^{CA}. Indeed, this was exactly what we found (Figure 3K). As $S1P_2$ supports mechanotransduction in endothelial cells (Jung et al., 2012), we then asked if it was activated by tensile stress in our system. We tested this by measuring ERK signaling, another downstream pathway of $S1P_2$ (Skoura and Hla, 2009). Baseline

(J) Effect of calyculin A on interaction between junctional E-cadherin and Gα12 measured by PLA fluorescence quantitation.

(K) Effect of Gα12 KD and reconstitution with GFP-Gα12^{WT} or GFP-Gα12^{CA} on stretch-induced junctional recruitment of p114 RhoGEF with or without S1P2 inhibitor (JTE-013).

Data are means ± SEM; n = 3 independent experiments. ****$p < 0.0001$, ***$p < 0.001$, **$p < 0.01$; n.s., not significant; unpaired t test (A and J) with Welch's correction or two-way ANOVA (B–H) with Sidak's multiple comparisons test.

levels of activated ERK (pERK) were substantially inhibited by JTE-013, confirming that this $S1P_2$ pathway was active in Caco-2 cells (Figures S3L and S3M), likely responding to S1P found in serum (Maceyka et al., 2012). But neither pERK levels nor the JTE-013-sensitive fraction were increased by calyculin. Overall, this suggested that, rather than being itself activated by mechanical stress, $S1P_2$ plays a facilitative role in tension-activated RhoA signaling, potentially by providing a pool of active Gα12 that could be recruited by E-cadherin.

Myosin VI Is a Force Sensor at the ZA

We then sought to identify the mechanosensor responsible for activating the Gα12-p114 RhoGEF-RhoA pathway in response to tensile stress. We focused our attention on Myosin VI, an F-actin-binding motor that is found at steady-state AJs and which can directly bind the cytoplasmic tail of E-cadherin (Mangold et al., 2012; Maddugoda et al., 2007). Importantly, Myosin VI has an intrinsic force sensitivity (Chuan et al., 2011; Oguchi et al., 2008; Altman et al., 2004). Under low loads, dimeric Myosin VI serves as a processive motor, but it can convert to a dynamic F-actin-based anchor when a sufficient load is applied (Chuan et al., 2011). We postulated that this property might allow cadherin-bound Myosin VI to respond to tensile forces at the ZA. Specifically, we hypothesized that Myosin VI might interact relatively transiently with E-cadherin under steady-state conditions but be stabilized through load-sensitive anchorage when tensile forces were transmitted through E-cadherin. Consistent with this, junctional Myosin VI levels were increased when monolayer tension was increased (Figures 4A–4C and S4A), and FRAP studies showed that calyculin stabilized Myosin VI-GFP at the ZA (Figures 4D and S4B; Table S1). Calyculin also increased the amount of Myosin VI that co-precipitated with E-cadherin-GFP (Figures 4E, 4F, and S4D), as well as the interaction between the endogenous proteins at the ZA detected by PLA (Figures 4G and S4E). Thus, tensile stress in monolayers enhances the association with E-cadherin that recruits Myosin VI to junctions (Maddugoda et al., 2007).

To test whether this might involve the intrinsic force sensitivity of Myosin VI, we sought to specifically disrupt this property while retaining the transport function of the motor. Force sensitivity in Myosin VI is thought to arise from mechanical gating of nucleotide exchange. Applied load has been reported to accelerate ADP binding, driving a transition from transport to anchoring in dimers (Chuan et al., 2011; Altman et al., 2004). Force-dependent inhibition of ADP release (Elting et al., 2011; Dunn et al., 2010) and acceleration of ATP binding (Sweeney et al., 2007) have also been proposed as mechanisms for coordinating heads via intramolecular strain. The insert 1 region of the motor is implicated in nucleotide gating, and a point mutant in this region (Myosin VI^{L310G}) affects nucleotide exchange and abolishes ATPase gating in the dimer (Pylypenko et al., 2011). However, this mutant preserves processive transport function, with only minor reductions in processive run length (Pylypenko et al., 2015).

We therefore hypothesized that the L310G mutation would specifically affect load-dependent anchoring by Myosin VI *in vivo*. So, we reconstituted Myosin VI KD cells with Myosin VI^{L310G} to test if this mutation affected its tension-sensitive recruitment (Figure S4F). In contrast to GFP-Myosin VI^{WT}, GFP-Myosin VI^{L310G} was not recruited to junctions (Figure S4A) or stabilized in response to calyculin (Figures 4D and S4C; Table S1). As seen for the endogenous protein, calyculin increased the association of GFP-Myosin VI^{WT} with E-cadherin, and this effectively required the cargo-binding domain that binds E-cadherin (Myosin $VI^{\Delta C}$) (Mangold et al., 2012). In contrast, while GFP-Myosin VI^{L310G} interacted with E-cadherin under baseline conditions, its association did not increase with calyculin (Figures 4H and 4I). Therefore, processive motor function, which is retained in Myosin VI^{L310G}, is not sufficient for tension-induced junctional recruitment. Instead, these findings suggest that recruitment of Myosin VI reflects its load-sensitive anchorage mediated by nucleotide gating.

Myosin VI Mediates Tension-Activated RhoA Signaling

Interestingly, junctional recruitment of Myosin VI preceded the accumulation of AHPH when cells were stimulated with calyculin (Figure S5A). This suggested that Myosin VI might be an upstream element in the tension-induced RhoA-activation pathway. Indeed, Myosin VI RNAi abolished the tension-induced increase in junctional RhoA, monitored with either the AHPH (Figures 5A and 5B) or RhoA FRET sensors (Figures 5C and S5B). Consistent with its acting at an upstream point, Myosin VI KD also compromised the tension-induced recruitment of Gα12 (Figures 5D and 5E) and p114 RhoGEF (Figures S5C and S5D). In contrast, p114 RhoGEF KD did not affect tension-sensitive recruitment (Figure S5E) or stabilization (Figure 4D) of Myosin VI. All these features were restored by Myosin VI^{WT} but not by GFP-Myosin VI^{L310G}, implying that its intrinsic mechanosensitivity was necessary for Myosin VI to participate in RhoA activation.

How, then, did Myosin VI promote junctional recruitment of the Gα12-p114 RhoGEF apparatus? Since Myosin VI can interact with E-cadherin, we considered whether it might promote the association between E-cadherin and Gα12. Indeed, more Gα12 co-immunoprecipitated with E-cadherin when monolayers were treated with calyculin, and this was reduced by Myosin VI KD (Figures 5G, 5H, and S5F). Similarly, Myosin VI KD reduced the calyculin-stimulated association between Gα12 and E-cadherin detected at junctions by PLA (Figure 5F). Myosin VI^{WT} restored the biochemical interaction between E-cadherin and Gα12 but not either Myosin $VI^{\Delta C}$ or Myosin VI^{L310G} (Figures 5G and 5H). Thus, both the intrinsic load sensitivity of Myosin VI and its ability to bind E-cadherin were necessary for tensile stress to enhance the E-cadherin-Gα12 interaction. As Myosin VI was also found in the E-cadherin immune complexes, it was formally possible that Myosin VI might independently recruit Gα12. However, the association between Myosin VI and Gα12 required E-cadherin, being reduced by E-cadherin KD (Figures S5G–S5I). This suggested that Myosin VI interacts indirectly with Gα12 through E-cadherin. Overall, these data suggest that Myosin VI couples force sensing to signal transduction by promoting the formation of the E-cadherin-Gα12 complex.

Gα12-p114 RhoGEF Signaling Helps Monolayers Resist Tensile Stress

Altogether, these findings identified a mechanosensitive RhoA pathway at AJs that responds when tensile stress is applied to monolayers. To evaluate its functional significance, we first tested how the epithelial barrier, measured by transepithelial

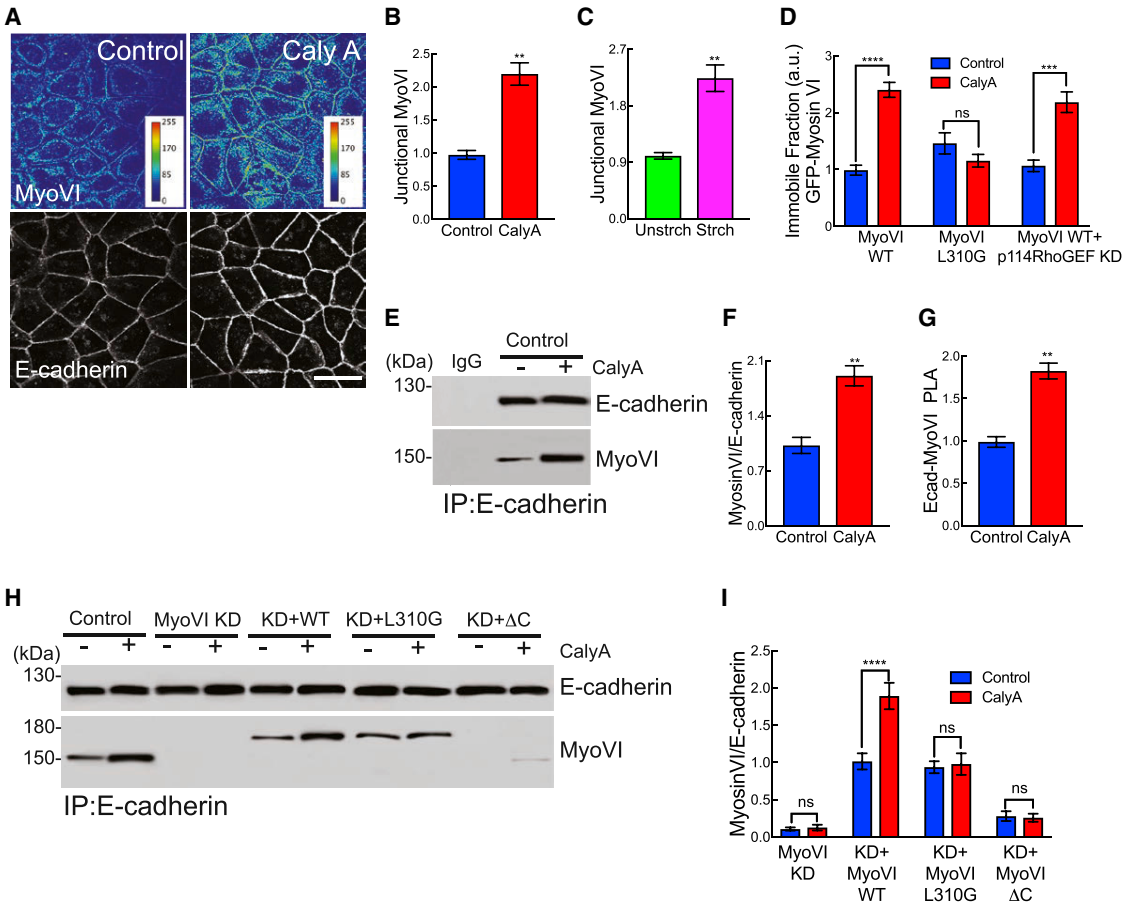

Figure 4. Myosin VI Recruits to E-Cadherin in Response to Tensile Monolayer Stress

(A–C) Effect of calyculin A (A and B) and mechanical stretch on junctional myosin VI (C). Representative images of Myosin VI and E-cadherin immunofluorescence (A) and quantitation (B and C).

(D) Effect of calyculin and p114 RhoGEF RNAi on junctional stability of GFP-Myosin VI^{WT} or GFP-Myosin VI^{L310G} (immobile fraction from FRAP normalized to controls).

(E and F) Effect of calyculin A on co-immunoprecipitation of endogenous Myosin VI with endogenous E-cadherin: representative blot (E) and quantitation (F).

(G) Calyculin A increases the PLA reaction between junctional E-cadherin and Myosin VI.

(H and I) Effect of calyculin A on co-immunoprecipitation of GFP-Myosin VI transgenes expressed in Myosin VI RNAi cells with E-cadherin (see text for details): representative blot (H) and quantitation (I).

Data are means ± SEM; n = 3 independent experiments. ****$p < 0.0001$, ***$p < 0.001$, **$p < 0.01$; n.s., not significant; unpaired t test (B, C, F, and G) with Welch's correction or two-way ANOVA (D and I) with Sidak's multiple comparisons test. Scale bar: 20 μm (A).

electrical resistance (TEER) of monolayers grown on Transwell filters, responded when intrinsic tension was increased with calyculin. TEER was effectively preserved in control monolayers, even when they were treated with calyculin (Figures 6A and S6A). The TEER of unstimulated p114 RhoGEF KD cells was marginally lower than in controls, comparable to what was observed with C3-T (Figure 6A) and reported earlier (Terry et al., 2011). Dramatically, TEER rapidly and progressively fell when calyculin was added to p114 RhoGEF KD cells or Gα12 KD cells (Figures 6A and S6A). The implication that RhoA signaling was necessary to preserve the epithelial barrier in the face of tensile stress was further supported by blocking RhoA directly with C3-T (Figures 6A and S6A). Together, these findings suggested that the tension-activated RhoA pathway was necessary to preserve epithelial barrier integrity in the face of mechanical stress.

To better characterize this process, we monitored E-cad-GFP junctions by live-imaging cells grown on glass substrata. Monolayer integrity remained undisturbed in both control Caco-2 cells and p114 RhoGEF KD cells (Video S3) that were not treated with calyculin (Figure 6C). In contrast, calyculin caused p114 RhoGEF KD cells to fracture at multiple sites throughout the monolayer during the course of the videos (Figure 6B and Video S3). Although fracturing was eventually seen in control monolayers treated with calyculin (Video S1), quantitation confirmed that it occurred much earlier in p114 RhoGEF KD cells (Figure 6C). Consistent with these calyculin-induced fractures being due to increased tension, the fracture incidence was reduced if p114 RhoGEF KD cells were first treated with the ROCK-inhibitor, Y-27632 (Figures 6D and S6B), which blocked the ability of calyculin to increase Myosin II phosphorylation and increase junctional tension (Figures S1A, S1B, and S1D). Similarly, Gα12 KD

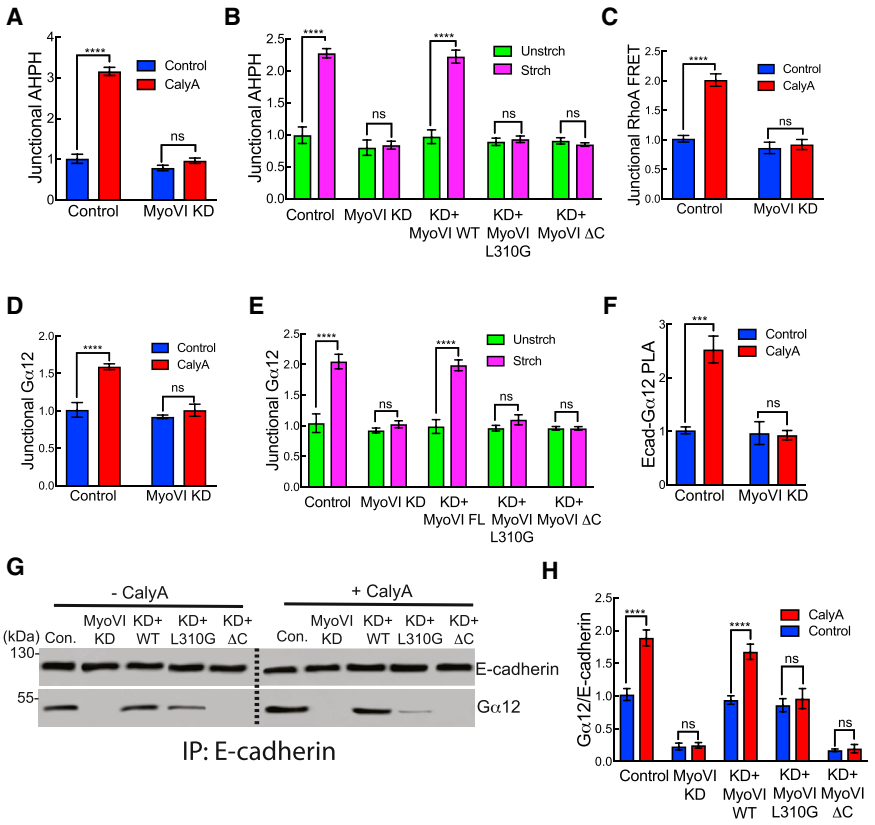

Figure 5. Myosin VI Supports Tension-Activated Junctional RhoA Signaling

(A) Effect of Myosin VI KD on calyculin-activated junctional GTP-RhoA measured by AHPH fluorescence quantitation.

(B) Effect of Myosin VI KD and reconstitution on stretch-activated junctional GTP-RhoA measured by AHPH fluorescence quantitation.

(C) Myosin VI KD reduces calyculin-activated junctional RhoA signaling measured by RhoA-FRET index.

(D and E) Effect of Myosin VI KD (D and E) and reconstitution with Myosin VI transgenes (E) on junctional recruitment of Gα12 in response to calyculin A (D) or mechanical stretch (E).

(F) Myosin VI KD reduces the calyculin-induced association of junctional E-cadherin and Gα12 measured by PLA fluorescence quantitation.

(G and H) Effect of Myosin VI mutations on the calyculin-stimulated association of GFP-Gα12 and E-cadherin; transgenes were expressed in Myosin VI RNAi cells: representative immunoblot (G) and quantitation (H).

Data are means ± SEM; n = 3 independent experiments. ****p < 0.0001, ***p < 0.001; n.s., not significant; two-way ANOVA (A–F and H) with Sidak's multiple comparisons test.

predisposed monolayers to fracture when stimulated with calyculin (Figure 6E). Collectively, these findings indicated that the tension-activated Gα12-p114 RhoGEF pathway serves to preserve the integrity of cell-cell contacts against the increased mechanical stress within the monolayers.

p114 RhoGEF Signaling Increases Tensile Strength of Monolayers

We then used the vertex model to consider how tension-activated p114 RhoGEF signaling might alter cell mechanics to maintain epithelial integrity (Computational Supplement, Data S1). One possibility was that p114 RhoGEF signaling increased the stiffness of the junctional cortex, which was predicted to protect a tissue undergoing a stretch deformation by decreasing the bulk modulus while increasing the shear modulus of the tissue (Nestor-Bergmann et al., 2018b). Actomyosin contributes to cortical stiffness, and, indeed, junctional actomyosin increased when control monolayers were treated by calyculin, and this was compromised by p114 RhoGEF KD (Figures S6C and S6D). Modeling an increase in junctional stiffness alone had little effect (Video S7), but when we incorporated an increase in internal contractility induced by calyculin, simulations revealed that if p114 RhoGEF signaling only increased cortical stiffness, then this accelerated the onset of fracture (Video S4), rather than delaying it, as was observed experimentally (Figure 6C). Thus, an increase in cortical stiffness alone did not explain the protective effect of p114 RhoGEF signaling.

Alternatively, we hypothesized that increased tensile strength of junctions (defined in the Computational Supplement, Data S1) might protect monolayers, even when cortical stiffness was also increased. Supporting this, simulations showed that increasing tensile strength via p114 RhoGEF signaling substantially delayed the onset of fracture (Figure S6E and Video S5), as was found in our experiments. To investigate how tensile strength might be increased, we then examined where fractures were initiated. Physical considerations predicted that forces would be concentrated at multicellular vertices (Higashi and Miller, 2017), which may be most prone to fracture. Indeed, α-18 staining increased at vertices after calyculin (Figure 6F), and E-Cad-GFP videos confirmed that calyculin-induced fractures began overwhelmingly at vertices in both control and p114 RhoGEF KD cells (Figure 6G). Close inspection of the videos indicated that cells separated from one another as fractures began (Figure S6F and Video S6), suggesting a defect in adhesion. E-cadherin intensity increased at vertices when control monolayers were treated with calyculin but not in p114 RhoGEF KD cells (Figures 6H and S6G). FRAP further showed that the immobile fraction of E-cadherin-GFP was reduced when p114 RhoGEF KD cells were treated with calyculin but maintained in control cells (Figure 6I).

This suggested that the tension-activated RhoA pathway that we have identified might increase the tensile strength of monolayers by reinforcing vertices against mechanical stress. Consistent with this, p114 RhoGEF, Gα12, and Myosin VI were all increased at vertices upon calyculin stimulation (Figure 6F), as they were at bicellular junctions. We then examined the actomyosin cytoskeleton as a potential way for enhanced RhoA signaling to support cadherin adhesion at the vertices. A role for NMII activation seemed unlikely, as it appeared to be maximally stimulated by calyculin, consistent with phosphatase

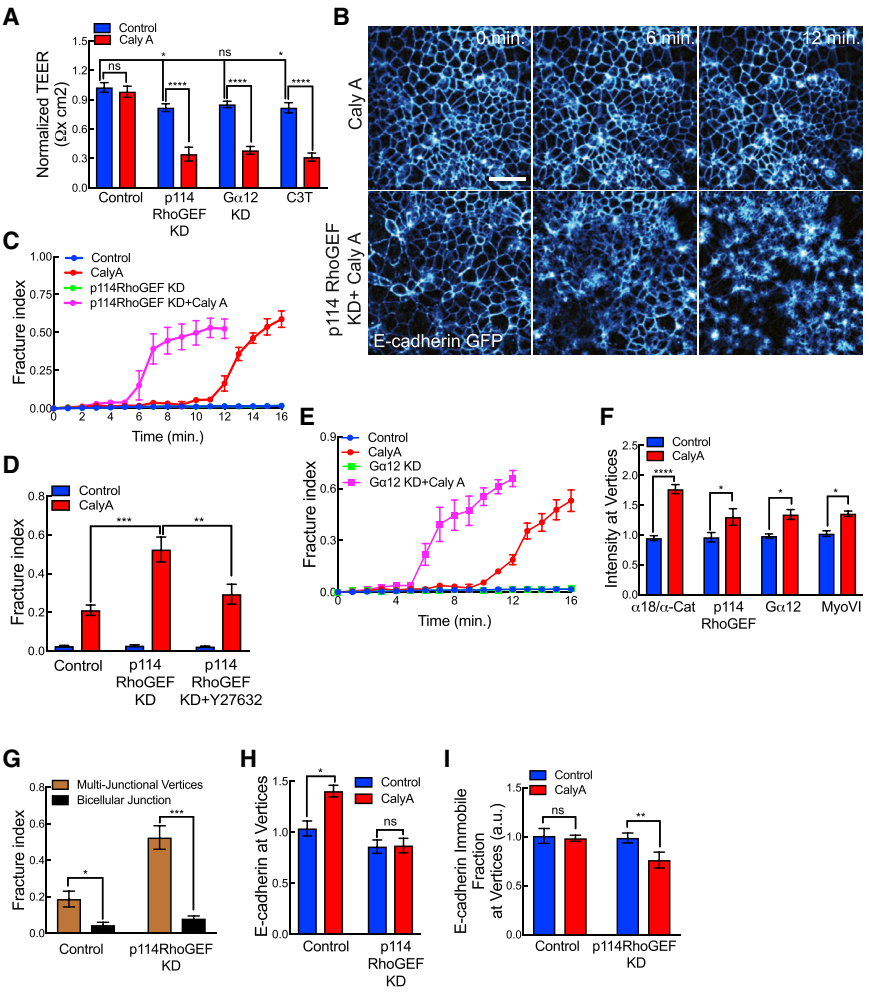

Figure 6. Tension-Activated Junctional RhoA Signaling Preserves Epithelial Integrity

(A) Effect of p114 RhoGEF KD, Gα12 KD, and C3T on epithelial transepithelial electrical resistance (TEER) after stimulation with calyculin A. Monolayers were grown for 21 days, pre-treated with C3T as appropriate (1 hr), then stimulated with calyculin (15 min) before TEER was measured; control was buffer alone.

(B and C) Effect of p114 RhoGEF KD on monolayer integrity after calyculin A. Representative stills from E-cadherin-GFP videos (B; corresponding videos are Video S1 and Video S3) and quantitation (C; drugs added at t = 0 min). See STAR Methods and Computational Supplement (Data S1) for details of fracture index.

(D) Effect of Y27632 on sensitivity of monolayers to fracture following calyculin A. Cells were pre-incubated with Y27632 for 1 hr before adding calyculin. Fracture index was measured 12 min after calyculin.

(E) Effect of Gα12 KD on sensitivity of monolayers to fracture following calyculin A treatment (drug added at t = 0 min).

(F) Effect of calyculin A on immunofluorescence intensity at multicellular vertices of α18 mAb (normalized to total junctional αE-Catenin), p114 RhoGEF, Gα12, and Myosin VI.

(G) Sites of fracture initiation (vertices or bicellular junctions) in control or p114 RhoGEF KD cells were quantitated in E-cadherin-GFP videos monitored for 12 min after adding calyculin.

(H) Effect of p114 RhoGEF KD on calyculin-induced accumulation of E-cadherin at multicellular vertices.

(I) Effect of p114 RhoGEF KD on E-cadherin-GFP stability (immobile fraction, FRAP) at multicellular vertices after calyculin stimulation.

Data are means ± SEM; n = 3 independent experiments. ****p < 0.0001, ***p < 0.001, **p < 0.01, *p < 0.05; n.s., not significant; two-way ANOVA (A, D, and F–I) with Sidak's multiple comparisons test, One-way ANOVA with Dunnett's multiple comparison test (A; only for control TEER analysis). Scale bar: 60 μm (B).

inhibition (Giannone et al., 2007; Vallotton et al., 2004), and not further affected by p114 RhoGEF KD (Figures S7A and S7B). In contrast, F-actin content at the vertices was increased when control cells were stimulated by calyculin (Figures 7A and 7B). SIM imaging showed that this manifested as a dense accumulation (Figure 7A), with increased nematic order (Q, Figures 7C and 7D), suggesting that F-actin organization was becoming more co-linear. In p114 RhoGEF KD cells, however, F-actin at vertices was more disorganized at baseline and failed to condense (Figures 7A and 7B) or increase in nematic order (Figure 7D) after calyculin. This suggested that the p114 RhoGEF signaling pathway stimulated actin assembly and organization at vertices.

One candidate to mediate this effect on F-actin was the formin mDia1, a RhoA effector that is active at AJs (Acharya et al., 2017; Rao and Zaidel-Bar, 2016; Carramusa et al., 2007; Sahai and Marshall, 2002). Indeed, calyculin increased mDia1 levels at vertices (Figures 7E and 7F) and bicellular junctions (Figure S7C) in control cells but not after p114 RhoGEF KD (Figures 7E, 7F, and S7C). Furthermore, mDia1 RNAi (Figure S7D) abolished the tension-induced accumulation of F-actin at vertices (Figures 7G and S7E) and blocked the ability of cells to increase E-cadherin and maintain its stable pool at vertices (Figures 7H and 7I). Finally, mDia1 KD also increased the sensitivity of monolayers to fracture when stimulated with calyculin (Figure 7J). Together, these findings suggest that F-actin regulation via mDia1 helps reinforce vertices to protect epithelial integrity against tensile stress.

DISCUSSION

Epithelia are subject to tensile forces that can challenge their cell-cell integrity (Charras and Yap, 2018). This is exemplified by our observation that monolayers fracture at junctions when monolayer contractility is acutely increased by calyculin. Similarly, overactivation of contractility during *Drosophila* gastrulation disrupts the actomyosin networks that couple cells together (Vasquez et al., 2014). Our experiments now identify a junctional mechanotransduction pathway that is responsible for sensing, and responding to, such tensile stresses. We propose that Myosin VI is the key sensor of acute tensile stress applied to AJs. It is stabilized and accumulates at AJs when tensile forces are transmitted to E-cadherin. This promotes the formation of an E-cadherin-Gα12 complex that activates the p114 RhoGEF-RhoA

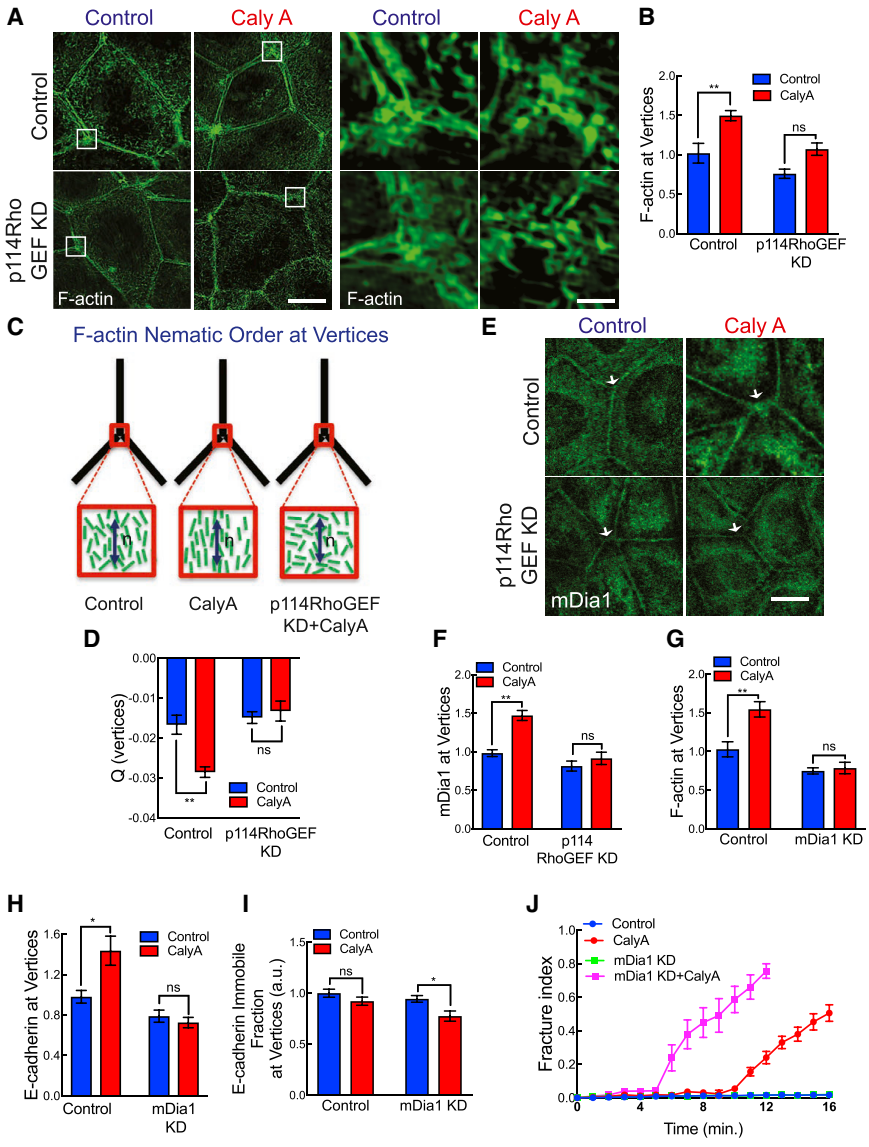

Figure 7. Tension-Activated RhoA Signaling Promotes Actin Assembly via mDia1 at Multicellular Vertices

(A) Effect of calyculin A and p114 RhoGEF RNAi on F-actin (phalloidin) immunofluorescence at cell-cell junctions imaged by SIM. Vertices (boxes) are enlarged in right-hand panels.

(B–D) Effect of p114 RhoGEF KD on fluorescence intensity (B) and nematic order (C and D) of F-actin at multicellular vertices in control and calyculin A-stimulated cells. (C) Cartoon of nematic order analysis represents the Q tensor alignment (green) along the nematic director (n vector, blue) in the image domain of a multicellular vertex (red box). Black bars represent the bicellular junctions that form the vertex.

(E and F) mDia1 immunofluorescence at multicellular vertices: effect of calyculin A and p114 RhoGEF KD. Representative images (E) and quantitation of fluorescence intensity (F).

(G–I) Effect of mDia1 KD on fluorescence intensity of F-actin (G) and E-cadherin (H) and E-cadherin-GFP stability (I; immobile fraction, FRAP) at multicellular vertices in control and calyculin A-stimulated cells.

(J) Effect of mDia1 KD on monolayer sensitivity to fracture in response to calyculin A (added at t = 0). Data are means ± SEM; n = 3 independent experiments. **p < 0.01, *p < 0.05; n.s., not significant; two-way ANOVA (A, D, and F–I) with Sidak's multiple comparisons test. Scale bars: 10 μm (A and E), 2 μm (A, inset).

pathway to increase the tensile strength of multicellular junctions via mDia1 (Figure S7F). Of note, RhoA signaling is active at the ZA, even under resting conditions (Ratheesh et al., 2012), but this is mediated by other GEFs such as Ect2. Thus, the Myosin VI-Gα12-p114 RhoGEF pathway that we have identified can be considered a selective response to superadded tensile stress.

At first sight, it seemed paradoxical that stimulation of RhoA would be used to preserve epithelial integrity. RhoA promotes actomyosin assembly at AJs under resting conditions (Ratheesh et al., 2012; Smutny et al., 2010) and also in calyculin-stimulated cells. Both F-actin and NMII increased at bicellular junctions upon treatment with calyculin, and this was abrogated by p114 RhoGEF KD. This p114 RhoGEF-stimulated increase in actomyosin might be expected to promote junctional rupture by increasing the line tension in bicellular junctions and enhancing the forces acting to disrupt epithelial integrity, especially those focused on multicellular junctions (Higashi and Miller, 2017; Choi et al., 2016). One possibility was that enhanced actomyosin also increased the stiffness of junctions to resist tensile stress. However, simulations in a mechanical model predicted that increasing stiffness alone would accelerate monolayer fracture rather than retarding it.

Instead, we consider that the protective effect of the p114 RhoGEF pathway is better explained by an increase in the tensile strength of AJs. In simulations of our vertex model, increasing tensile strength protected monolayer integrity against calyculin-induced stresses, even if junctional stiffness was also increased. Experimentally, we suggest that this protective effect is especially important at the multicellular vertices. Physical considerations identify vertices as the junctional sites where cellular forces will be greatest (Higashi and Miller, 2017), and, indeed, vertices were the principal sites where cell separation first began in our experiments. The accelerated onset of fracture that was seen in p114 RhoGEF KD cells thus implied that tension-activated p114 RhoGEF-RhoA signaling might reinforce vertices against stress.

RhoA signals to both NMII and F-actin (Lessey et al., 2012). However, calyculin appeared to maximally stimulate NMII, and this was not reduced by p114 RhoGEF KD. In contrast, p114 RhoGEF signaling was necessary to stimulate actin assembly at vertices in response to calyculin, an effect that was mediated by the RhoA-sensitive formin, mDia1. In turn, mDia1 was required to reinforce E-cadherin at vertices and for monolayers

to resist tensile stress. Thus, p114 RhoGEF-RhoA-mediated actin assembly appeared to be key to preserving epithelial integrity in our experiments, although NMII regulation may also be relevant when tension is increased by other means. Without excluding possible roles for other membrane proteins found at vertices (Higashi and Miller, 2017), we therefore propose that tension-activated RhoA signaling increases the tensile strength of monolayers by stimulating mDia1-dependent actin assembly to reinforce E-cadherin adhesion at vertices.

It was noteworthy that RhoA signaling was selectively increased at cell-cell junctions but not at other adhesive sites, especially cell-substrate interactions. This highlights a key role for mechanisms that can confer spatial specificity on the mechanotransduction response. Two elements appear to be responsible for junctional selectivity in this instance. First, Gα12 can interact directly with E-cadherin, and this is necessary for junctional RhoA to be stimulated by tensile stress. Our working model is that Gα12, preactivated by $S1P_2$, is recruited to E-cadherin upon application of mechanical stress, where it then recruits and activates p114 RhoGEF to drive RhoA signaling.

Second, we identified Myosin VI as the force sensor that promotes the E-cadherin-Gα12 association. This requires both the ability of Myosin VI to associate with E-cadherin and also its pronounced capacity to anchor to actin filaments in response to load (Chuan et al., 2011; Altman et al., 2004). Our findings suggest that Myosin VI interacts transiently with E-cadherin under steady-state conditions. However, it is stabilized by load-sensitive anchorage when acute tensile stresses are transmitted through E-cadherin. In contrast, the functional impact of Myosin VI was abrogated by the L310G mutant, which retains processive motor function but has defective nucleotide gating linked to load-sensitivity (Pylypenko et al., 2015; Pylypenko et al., 2011). How increased F-actin anchorage promotes association of Myosin VI with E-cadherin remains to be determined. One possibility is that the increased dwell time of Myosin VI facilitates post-translational modifications that stabilize its binding to E-cadherin. This stabilized Myosin VI-cadherin complex may then promote the recruitment of Gα12 through conformational changes or accessory proteins. Irrespective, Myosin VI appears to exert its signaling effects via E-cadherin-Gα12, since tension-activated RhoA was abolished if Gα12 was unable to bind cadherin.

In conclusion, our findings identify a mechanotransduction pathway that is selectively elicited to preserve epithelial integrity in response to tensile stress. The selectivity of this pathway implies that junctions may possess multiple mechanisms to sense mechanical signals that operate under different circumstances. Of note, α-catenin is necessary for the elemental force-sensitive association of cadherins with F-actin (Buckley et al., 2014) and also supports Ect 2-dependent RhoA signaling in steady-state AJs (Ratheesh et al., 2012). Therefore, α-catenin may confer mechanosensitivity under baseline conditions, whereas the Myosin VI-dependent pathway that we have identified is activated in response to superadded mechanical stress. Furthermore, our experiments tested the effects of acute application of tensile stress. Other mechanisms contribute when mechanical stresses are applied more slowly or are sustained longer, such as cellular rearrangements and oriented cell division (Hart et al., 2017; Etournay et al., 2015; Wyatt et al., 2015; Campinho et al., 2013). That epithelia possess such a diversity of compensatory mechanisms attests to the fundamental challenge of mechanical stress in epithelial biology.

STAR★METHODS

Detailed methods are provided in the online version of this paper and include the following:

- KEY RESOURCES TABLE
- CONTACT FOR REAGENT AND RESOURCE SHARING
- EXPERIMENTAL MODEL AND SUBJECT DETAILS
- METHOD DETAILS
  - Application of Equibiaxial Static Stretch
  - Transfection and Reagent Use
  - Plasmids
  - Immunofluorescence and Live-Cell Microscopy
  - Proximity Ligation Assay (PLA)
  - FRET and FRAP Analysis
  - Junctional Tension Measured by Recoil after Laser Ablation
  - Traction Force Microscopy (TFM) and Analysis of Internal Cellular Stress
  - Nematic Order Analysis of F-Actin
  - Immunoprecipitation and Immunoblotting
  - Transepithelial Electrical Resistance (TEER) Measurements
- QUANTIFICATION AND STATISTICAL ANALYSIS
  - Image Processing and Analysis
  - Statistical Analysis
- DATA AND SOFTWARE AVAILABILITY

SUPPLEMENTAL INFORMATION

Supplemental Information includes seven figures, two tables, seven videos, and one data file and can be found with this article online at https://doi.org/10.1016/j.devcel.2018.09.016.

ACKNOWLEDGMENTS

We thank all our laboratory colleagues for their support and advice; the many colleagues who provided reagents; and Benoit Ladoux and Vanesa Tomatis for their support in establishing TFM. This work was supported by grants (1037320, 1067405) and fellowships (1044041, 1136592) from the National Health and Medical Research Council of Australia, Australian Research Council (DP150101367 to A.S.Y. and FT160100366 to G.A.G.), Queensland Cancer Council (1086857, 1128123), and Human Frontiers Science Program (RGP0023/2014). Optical microscopy was performed at the ACRF/IMB Cancer Biology Imaging Facility, established with the generous support of the Australian Cancer Research Foundation and the Queensland Brain Institute microscopy facility supported by ARC LIEF grant (LE130100078). A.N.-B. was supported by a Company of Biologists, Journal of Cell Science, Travelling Fellowship (JCSTF-170805).

AUTHOR CONTRIBUTIONS

B.R.A., Z.B., and A.S.Y. conceived the project and designed the experiments. B.R.A. performed the experiments with the support of X.L. and K.D. A.N.-B. and O.E.J. performed the modeling. S.G. performed the TFM and BISM with the support of E.G. and G.A.G. (for TFM) and P.M. (for BISM). B.R.A., A.N.-B., and A.S.Y. wrote the paper.

DECLARATION OF INTERESTS

The authors declare no competing interests.

Received: March 12, 2018
Revised: July 16, 2018
Accepted: September 15, 2018
Published: October 11, 2018

SUPPORTING CITATIONS

The following references appear in the Supplemental Information (Data S1): Kursawe et al. (2017); Okuda et al. (2015); Sugimura and Ishihara (2013).

REFERENCES

Acharya, B.R., Wu, S.K., Lieu, Z.Z., Parton, R.G., Grill, S.W., Bershadsky, A.D., Gomez, G.A., and Yap, A.S. (2017). Mammalian diaphanous 1 mediates a pathway for E-cadherin to stabilize epithelial barriers through junctional contractility. Cell Rep. *18*, 2854–2867.

Altman, D., Sweeney, H.L., and Spudich, J.A. (2004). The mechanism of myosin VI translocation and its load-induced anchoring. Cell *116*, 737–749.

Buckley, C.D., Tan, J.L., Anderson, K.L., Hanein, D., Volkmann, N., Weis, W.I., Nelson, W.J., and Dunn, A.R. (2014). Cell adhesion. The minimal cadherin-catenin complex binds to actin filaments under force. Science *346*, 1254211.

Campinho, P., Behrndt, M., Ranft, J., Risler, T., Minc, N., and Heisenberg, C.P. (2013). Tension-oriented cell divisions limit anisotropic tissue tension in epithelial spreading during zebrafish epiboly. Nat. Cell Biol. *15*, 1405–1414.

Carramusa, L., Ballestrem, C., Zilberman, Y., and Bershadsky, A.D. (2007). Mammalian diaphanous-related formin Dia1 controls the organization of E-cadherin-mediated cell-cell junctions. J. Cell Sci. *120*, 3870–3882.

Charras, G.T., and Yap, A.S. (2018). Tensile forces and mechanotransduction at cell-cell junctions. Curr. Biol. *28*, R445–R457.

Choi, W., Acharya, B.R., Peyret, G., Fardin, M.A., Mège, R.M., Ladoux, B., Yap, A.S., Fanning, A.S., and Peifer, M. (2016). Remodeling the zonula adherens in response to tension and the role of afadin in this response. J. Cell Biol. *213*, 243–260.

Chuan, P., Spudich, J.A., and Dunn, A.R. (2011). Robust mechanosensing and tension generation by myosin VI. J. Mol. Biol. *405*, 105–112.

Dunn, A.R., Chuan, P., Bryant, Z., and Spudich, J.A. (2010). Contribution of the myosin VI tail domain to processive stepping and intramolecular tension sensing. Proc. Natl. Acad. Sci. U S A *107*, 7746–7750.

Elting, M.W., Bryant, Z., Liao, J.C., and Spudich, J.A. (2011). Detailed tuning of structure and intramolecular communication are dispensable for processive motion of myosin VI. Biophys. J. *100*, 430–439.

Etournay, R., Popović, M., Merkel, M., Nandi, A., Blasse, C., Aigouy, B., Brandl, H., Myers, G., Salbreux, G., Jülicher, F., et al. (2015). Interplay of cell dynamics and epithelial tension during morphogenesis of the Drosophila pupal wing. Elife *4*, e07090.

Farhadifar, R., Röper, J.C., Aigouy, B., Eaton, S., and Jülicher, F. (2007). The influence of cell mechanics, cell-cell interactions, and proliferation on epithelial packing. Curr. Biol. *17*, 2095–2104.

Fletcher, A.G., Osterfield, M., Baker, R.E., and Shvartsman, S.Y. (2014). Vertex models of epithelial morphogenesis. Biophys. J. *106*, 2291–2304.

Giannone, G., Dubin-Thaler, B.J., Rossier, O., Cai, Y., Chaga, O., Jiang, G., Beaver, W., Döbereiner, H.G., Freund, Y., Borisy, G., et al. (2007). Lamellipodial actin mechanically links myosin activity with adhesion-site formation. Cell *128*, 561–575.

Gomez, G.A., McLachlan, R.W., Wu, S.K., Caldwell, B.J., Moussa, E., Verma, S., Bastiani, M., Priya, R., Parton, R.G., Gaus, K., et al. (2015). An RPTPα/Src family kinase/Rap1 signaling module recruits myosin IIB to support contractile tension at apical E-cadherin junctions. Mol. Biol. Cell *26*, 1249–1262.

Goulimari, P., Kitzing, T.M., Knieling, H., Brandt, D.T., Offermanns, S., and Grosse, R. (2005). Galpha 12/13 is essential for directed cell migration and localized Rho-Dia1 function. J. Biol. Chem. *280*, 42242–42251.

Guilluy, C., Swaminathan, V., Garcia-Mata, R., O'Brien, E.T., Superfine, R., and Burridge, K. (2011). The Rho GEFs LARG and GEF-H1 regulate the mechanical response to force on integrins. Nat. Cell Biol. *13*, 722–727.

Harris, A.R., Daeden, A., and Charras, G.T. (2014). Formation of adherens junctions leads to the emergence of a tissue-level tension in epithelial monolayers. J. Cell Sci. *127*, 2507–2517.

Hart, K.C., Tan, J., Siemers, K.A., Sim, J.Y., Pruitt, B.L., Nelson, W.J., and Gloerich, M. (2017). E-cadherin and LGN align epithelial cell divisions with tissue tension independently of cell shape. Proc. Natl. Acad. Sci. U S A *114*, E5845–E5853.

Hasson, T., and Mooseker, M.S. (1994). Porcine Myosin-VI: characterization of a new mammalian unconventional myosin. J. Cell Biol. *127*, 425–440.

Higashi, T., and Miller, A.L. (2017). Tricellular junctions: how to build junctions at the TRICkiest points of epithelial cells. Mol. Biol. Cell *28*, 2023–2034.

Honda, H., and Eguchi, G. (1980). How much does the cell boundary contract in a monolayered cell sheet? J. Theor. Biol. *84*, 575–588.

Jung, B., Obinata, H., Galvani, S., Mendelson, K., Ding, B.S., Skoura, A., Kinzel, B., Brinkmann, V., Rafii, S., Evans, T., et al. (2012). Flow-regulated endothelial S1P receptor-1 signaling sustains vascular development. Dev. Cell *23*, 600–610.

Kaplan, D.D., Meigs, T.E., and Casey, P.J. (2001). Distinct regions of the cadherin cytoplasmic domain are essential for functional interaction with Galpha 12 and beta-catenin. J. Biol. Chem. *276*, 44037–44043.

Kerridge, S., Munjal, A., Philippe, J.M., Jha, A., de las Bayonas, A.G., Saurin, A.J., and Lecuit, T. (2016). Modular activation of Rho1 by GPCR signalling imparts polarized myosin II activation during morphogenesis. Nat. Cell Biol. *18*, 261–270.

Krakstad, B.F., Ardawatia, V.V., and Aragay, A.M. (2004). A role for Galpha12/Galpha13 in p120ctn regulation. Proc. Natl. Acad. Sci. U S A *101*, 10314–10319.

Kursawe, J., Baker, R.E., and Fletcher, A.G. (2017). Impact of implementation choices on quantitative predictions of cell-based computational models. J. Comp. Phys. *345*, 752–767.

le Duc, Q., Shi, Q., Blonk, I., Sonnenberg, A., Wang, N., Leckband, D., and de Rooij, J. (2010). Vinculin potentiates E-cadherin mechanosensing and is recruited to actin-anchored sites within adherens junctions in a myosin II-dependent manner. J. Cell Biol. *189*, 1107–1115.

Lecuit, T., and Lenne, P.F. (2007). Cell surface mechanics and the control of cell shape, tissue patterns and morphogenesis. Nat. Rev. Mol. Cell Biol. *8*, 633–644.

Lessey, E.C., Guilluy, C., and Burridge, K. (2012). From mechanical force to RhoA activation. Biochemistry *51*, 7420–7432.

Levine, E., Lee, C.H., Kintner, C., and Gumbiner, B.M. (1994). Selective disruption of E-cadherin function in early Xenopus embryos by a dominant negative mutant. Development *120*, 901–909.

Liang, X., Budnar, S., Gupta, S., Verma, S., Han, S.P., Hill, M.M., Daly, R.J., Parton, R.G., Hamilton, N.A., Gomez, G.A., et al. (2017). Tyrosine dephosphorylated cortactin downregulates contractility at the epithelial zonula adherens through SRGAP1. Nat. Commun. *8*, 790.

Lin, F., Chen, S., Sepich, D.S., Panizzi, J.R., Clendenon, S.G., Marrs, J.A., Hamm, H.E., and Solnica-Krezel, L. (2009). Galpha12/13 regulate epiboly by inhibiting E-cadherin activity and modulating the actin cytoskeleton. J. Cell Biol. *184*, 909–921.

Maceyka, M., Harikumar, K.B., Milstien, S., and Spiegel, S. (2012). Sphingosine-1-phosphate signaling and its role in disease. Trends Cell Biol. *22*, 50–60.

Maddugoda, M.P., Crampton, M.S., Shewan, A.M., and Yap, A.S. (2007). Myosin VI and vinculin cooperate during the morphogenesis of cadherin cell cell contacts in mammalian epithelial cells. J. Cell Biol. *178*, 529–540.

Mangold, S., Norwood, S.J., Yap, A.S., and Collins, B.M. (2012). The juxtamembrane domain of the E-cadherin cytoplasmic tail contributes to its interaction with myosin VI. Bioarchitecture *2*, 185–188.

Manibog, K., Li, H., Rakshit, S., and Sivasankar, S. (2014). Resolving the molecular mechanism of cadherin catch bond formation. Nat. Commun. *5*, 3941.

Martin, J.W., Cavagnini, K.S., Brawley, D.N., Berkley, C.Y., Smolski, W.C., Garcia, R.D., Towne, A.L., Sims, J.R., and Meigs, T.E. (2016). A Ga12-specific binding domain in AKAP-Lbc and p114RhoGEF. J. Mol. Signal. *11*, 1–17.

Meigs, T.E., Fields, T.A., McKee, D.D., and Casey, P.J. (2001). Interaction of Galpha 12 and Galpha 13 with the cytoplasmic domain of cadherin provides a mechanism for beta -catenin release. Proc. Natl. Acad. Sci. U S A *98*, 519–524.

Meigs, T.E., Juneja, J., DeMarco, C.T., Stemmle, L.N., Kaplan, D.D., and Casey, P.J. (2005). Selective uncoupling of G alpha 12 from Rho-mediated signaling. J. Biol. Chem. *280*, 18049–18055.

Michael, M., Meiring, J.C.M., Acharya, B.R., Matthews, D.R., Verma, S., Han, S.P., Hill, M.M., Parton, R.G., Gomez, G.A., and Yap, A.S. (2016). Coronin 1B reorganizes the architecture of F-actin networks for contractility at steady-state and apoptotic adherens junctions. Dev. Cell *37*, 58–71.

Nagai, T., and Honda, H. (2001). A dynamic cell model for the formation of epithelial tissues. Philos. Mag. B *81*, 699–719.

Nestor-Bergmann, A., Goddard, G., Woolner, S., and Jensen, O.E. (2018a). Relating cell shape and mechanical stress in a spatially disordered epithelium using a vertex-based model. Math. Med. Biol. *35*, 1–27.

Nestor-Bergmann, A., Johns, S., Woolner, S., and Jensen, O.E. (2018b). Mechanical characterization of disordered and anisotropic cellular monolayers. Phys. Rev. E *97*, 052409, https://doi.org/10.1103/PhysRevE.97.052409.

Nestor-Bergmann, A., Stooke-Vaughn, G.A., Goddard, G.K., Starborg, T., Jensen, O.E., and Woolner, S. (2018c). Decoupling the roles of cell shape and mechanical stress in orienting and cueing epithelial mitosis. bioRxiv, 177592, https://doi.org/10.1101/177592.

Nier, V., Jain, S., Lim, C.T., Ishihara, S., Ladoux, B., and Marcq, P. (2016). Inference of internal stress in a cell monolayer. Biophys. J. *110*, 1625–1635.

Oguchi, Y., Mikhailenko, S.V., Ohki, T., Olivares, A.O., De La Cruz, E.M., and Ishiwata, S. (2008). Load-dependent ADP binding to myosins V and VI: implications for subunit coordination and function. Proc. Natl. Acad. Sci. U S A *105*, 7714–7719.

Okuda, S., Inoue, Y., Eiraku, M., Adachi, T., and Sasai, Y. (2015). Vertex dynamics simulations of viscosity-dependent deformation during tissue morphogenesis. Biomech. Model. Mechanobiol. *14*, 413–425.

Oldham, W.M., and Hamm, H.E. (2008). Heterotrimeric G protein activation by G-protein-coupled receptors. Nat. Rev. Mol. Cell Biol. *9*, 60–71.

Pertz, O., Hodgson, L., Klemke, R.L., and Hahn, K.M. (2006). Spatiotemporal dynamics of RhoA activity in migrating cells. Nature *440*, 1069–1072.

Piekny, A.J., and Glotzer, M. (2008). Anillin is a scaffold protein that links RhoA, actin, and myosin during cytokinesis. Curr. Biol. *18*, 30–36.

Priya, R., Gomez, G.A., Budnar, S., Verma, S., Cox, H.L., Hamilton, N.A., and Yap, A.S. (2015). Feedback regulation through myosin II confers robustness on RhoA signalling at E-cadherin junctions. Nat. Cell Biol. *17*, 1282–1293.

Pruitt, B.L., Dunn, A.R., Weis, W.I., and Nelson, W.J. (2014). Mechano-transduction: from molecules to tissues. PLoS Biol. *12*, e1001996.

Pylypenko, O., Song, L., Shima, A., Yang, Z., Houdusse, A.M., and Sweeney, H.L. (2015). Myosin VI deafness mutation prevents the initiation of processive runs on actin. Proc. Natl. Acad. Sci. U S A *112*, E1201–E1209.

Pylypenko, O., Song, L., Squires, G., Liu, X., Zong, A.B., Houdusse, A., and Sweeney, H.L. (2011). Role of insert-1 of myosin VI in modulating nucleotide affinity. J. Biol. Chem. *286*, 11716–11723.

Rao, M.V., and Zaidel-Bar, R. (2016). Formin-mediated actin polymerization at cell-cell junctions stabilizes E-cadherin and maintains monolayer integrity during wound repair. Mol. Biol. Cell *27*, 2844–2856.

Ratheesh, A., Gomez, G.A., Priya, R., Verma, S., Kovacs, E.M., Jiang, K., Brown, N.H., Akhmanova, A., Stehbens, S.J., and Yap, A.S. (2012). Centralspindlin and alpha-catenin regulate Rho signalling at the epithelial zonula adherens. Nat. Cell Biol. *14*, 818–828.

Reymann, A.C., Staniscia, F., Erzberger, A., Salbreux, G., and Grill, S.W. (2016). Cortical flow aligns actin filaments to form a furrow. Elife *5*, e17807, https://doi.org/10.7554/eLife.17807.

Sahai, E., and Marshall, C.J. (2002). ROCK and Dia have opposing effects on adherens junctions downstream of Rho. Nat. Cell Biol. *4*, 408–415.

Saw, T.B., Doostmohammadi, A., Nier, V., Kocgozlu, L., Thampi, S., Toyama, Y., Marcq, P., Lim, C.T., Yeomans, J.M., and Ladoux, B. (2017). Topological defects in epithelia govern cell death and extrusion. Nature *544*, 212–216.

Siehler, S. (2009). Regulation of RhoGEF proteins by G12/13-coupled receptors. Br. J. Pharmacol *158*, 41–49.

Skoura, A., and Hla, T. (2009). Regulation of vascular physiology and pathology by the S1P2 receptor subtype. Cardiovasc. Res. *82*, 221–228.

Smutny, M., Cox, H.L., Leerberg, J.M., Kovacs, E.M., Conti, M.A., Ferguson, C., Hamilton, N.A., Parton, R.G., Adelstein, R.S., and Yap, A.S. (2010). Myosin II isoforms identify distinct functional modules that support integrity of the epithelial zonula adherens. Nat. Cell Biol. *12*, 696–702.

Sugimura, K., and Ishihara, S. (2013). The mechanical anisotropy in a tissue promotes ordering in hexagonal cell packing. Development *140*, 4091–4101.

Sweeney, H.L., Park, H., Zong, A.B., Yang, Z., Selvin, P.R., and Rosenfeld, S.S. (2007). How myosin VI coordinates its heads during processive movement. EMBO J. *26*, 2682–2692.

Terry, S.J., Zihni, C., Elbediwy, A., Vitiello, E., Leefa Chong San, I.V., Balda, M.S., and Matter, K. (2011). Spatially restricted activation of RhoA signalling at epithelial junctions by p114RhoGEF drives junction formation and morphogenesis. Nat. Cell Biol. *13*, 159–166.

Tsuji, T., Ohta, Y., Kanno, Y., Ohashi, K., and Mizuno, K. (2011). Involvement of p114-RhoGEF and Lfc in Wnt-3a- and dishevelled-induced RhoA activation and neurite retraction in N1E-115 mouse neuroblastoma cells. Mol. Biol. Cell *21*, 3590–3600.

Vallotton, P., Gupton, S.L., Waterman-Storer, C.M., and Danuser, G. (2004). Simultaneous mapping of filamentous actin flow and turnover in migrating cells by quantitative fluorescent speckle microscopy. Proc. Natl. Acad. Sci. U S A *101*, 9660–9665.

Vasquez, C.G., Tworoger, M., and Martin, A.C. (2014). Dynamic myosin phosphorylation regulates contractile pulses and tissue integrity during epithelial morphogenesis. J. Cell Biol. *206*, 435–450.

Wyatt, T.P., Harris, A.R., Lam, M., Cheng, Q., Bellis, J., Dimitracopoulos, A., Kabla, A.J., Charras, G.T., and Baum, B. (2015). Emergence of homeostatic epithelial packing and stress dissipation through divisions oriented along the long cell axis. Proc. Natl. Acad. Sci. U S A *112*, 5726–5731.

Yap, A.S., Duszyc, K., and Viasnoff, V. (2018). Mechanosensing and mechanotransduction at cell-cell junctions. Cold Spring Harb. Perspect. Biol. *10*, https://doi.org/10.1101/cshperspect.a028761.

Yonemura, S., Wada, Y., Watanabe, T., Nagafuchi, A., and Shibata, M. (2010). Alpha-catenin as a tension transducer that induces adherens junction development. Nat. Cell Biol. *12*, 533–542.

STAR★METHODS

KEY RESOURCES TABLE

REAGENT or RESOURCE	SOURCE	IDENTIFIER
Antibodies		
Rabbit polyclonal Phospho-Myosin Light Chain 2 (Thr18/Ser19) Antibody	Cell Signaling Technology	Cat# 3674; RRID: AB_2147464
Mouse monoclonal Myosin Light Chain 2 antibody [AT3B2]	Abcam	Cat# ab89594; RRID: AB_2042414
Rabbit polyclonal Alpha Catenin antibody	Thermo Fisher Scientific	Cat# 71-1200; RRID: AB_2533974
Rat polyclonal Alpha Catenin (alpha 18) antibody	Gift from Dr. Akira Nagafuchi, Nara Medical University, Japan	Nat. Cell Biol. (2010), 12(6), 533-42. PMID: 20453849
Goat polyclonal p114RhoGEF antibody	Abcam	Cat# ab10152; RRID: AB_296885
Rabbit polyclonal p114RhoGEF antibody	Abcam	Cat# ab96520; RRID: AB_10680897
Rabbit polyclonal Gα12 antibody	Abcam	Cat# ab236617
Rabbit polyclonal Gα12 antibody	Abcam	Cat# ab154004
Rabbit polyclonal Gα13 antibody	Abcam	Cat# ab128900
Rabbit polyclonal GEFH1 antibody	Abcam	Cat# ab155785
Mouse monoclonal LARG antibody	Merck-Millipore	Cat#MABT124
Rabbit polyclonal ECT2 antibody	Merck-Millipore	Cat# 07-1364; RRID: AB_10805932
Rabbit monoclonal p115RhoGEF antibody	Cell Signaling Technology	Cat# 3669S; RRID: AB_2059739
Rabbit myosin VI antibody	Generated in lab, *for details see citation*.	J. Cell Biol. (2007), 178(3), 529-540. PMID: 17664339
Mouse monoclonal myosin VI antibody	Sigma-Aldrich	Cat# M0691; RRID: AB_477166
Rat monoclonal E-cadherin (ECCD-2) antibody	Thermo Fisher Scientific	Cat# 13-1900; RRID: AB_2533005
Mouse monoclonal E-cadherin (HECD1) antibody	Gift from Dr. M. Wheelock, University of Nebraska, USA, with permission from Drs. Masatoshi Takeichi, RIKEN CBD, Japan	J. Cell Biol. (1989), 109(4 Pt 1), 1787-1794. PMID: 2793940
Mouse monoclonal GFP antibody	Roche	Cat# 11814460001; RRID: AB_390913
Alexa Fluor® 647 Phalloidin antibody	Thermo Fisher Scientific	Cat# A22287; RRID: AB_2620155
Alex Fluor 546 Phalloidin antibody	Thermo Fisher Scientific	Cat# A-22283; RRID: AB_2632953
Chemicals, Peptides, and Recombinant Proteins		
Calyculin A (Phosphatase inhititor)	Abcam	Cat# ab141784
Y27632 (ROCK inhibitor)	Sigma-Aldrich	Cat#Y0503
C3 Transferase (RhoA inhibitor)	Cytoskeleton Inc	Cat#CT04-A
JTE-013 (S1P2-GPCR inhibitor)	Sigma-Aldrich	Cat# J4080
CYM50358 (S1P4-GPCR inhibitor)	Sigma-Aldrich	Cat# SML1066
W146 Hydrate (S1P1-GPCR inhibitor)	Sigma-Aldrich	Cat# W1020
H2L5186303 (LPA2-GPCR inhibitor)	Sigma-Aldrich	Cat# SML0989
Ki-16425 (LPA1 & 3-GPCR inhibitor)	Sigma-Aldrich	Cat# SML0971
FR-171113 (PAR1-GPCR inhibitor)	Sigma-Aldrich	Cat# SML0028
ML354 (PAR4-GPCR inhibitor)	Sigma-Aldrich	Cat# SML1439
Experimental Models: Cell Lines		
$Caco_2$ Cell (Human Colorectal Adenocarcinoma cells)	ATCC	Cat# HTB-37, RRID:CVCL_0025
Oligonucleotides		
p114RhoGEF Y260A Mutagenesis primer (Sense) 5'-GCAGGTTCCTTGAAAGACCCggTGTTAGATGACCAT GGAGAC-3'	IDT, Singapore	Custom Designed
p114RhoGEF Y260A Mutagenesis primer (Antisense) 5'-GTCTCCATGGTCATCTAACACCGGGTCTTTCAAGG AACCTGC -3'	IDT, Singapore	Custom Designed

(*Continued on next page*)

Continued

REAGENT or RESOURCE	SOURCE	IDENTIFIER
Myosin VI L310G Mutagenesis primers (Sense) 5'-CACAACGCATAACCAAAggCCCAGTGCTGGTG GAGC-3'	IDT, Singapore	Custom Designed
Myosin VI L310G Mutagenesis primers (Antisense) 5'-GCTCCACCAGCACTGGGCCTTTGGTTATGCGT TGTG-3'	IDT, Singapore	Custom Designed
Gα12 L231Q Mutagenesis primers (Sense) 5'-TGTGGGCGGCcagCGGTCCCAG-3'	IDT, Singapore	Custom Designed
Gα12 L231Q Mutagenesis primers (Antisense) 5'-TCCACCATCTTAAAGGGGATCTTCTTAATAACGAA GTCATGCTCCA-3'	IDT, Singapore	Custom Designed
See Table S2 for siRNA sequences used in the study.	N/A	N/A
Recombinant DNA		
GFP–AHPH	Gift from Dr. M. Glotzer, University of Chicago, USA	Piekny et al. (2008) PMID: 18158243
pTriEx-RhoA FRET WT biosensor	Addgene	Plasmid#12150 Pertz et al. (2006). PMID: 16547516
CFP-p114RhoGEF	Gift from Dr. K. Mizuno, Tohoku University; Japan	Tsuji et al. (2011). PMID: 20810787
CFP-p114RhoGEF Y260A	Adapted from Terry, et. al., Nat Cell Biol, 2011.	Terry et al. (2011). PMID: 21258369
G protein-alpha 12 FL (Q231L)	Addgene	Plasmid#46825
GFP-G protein-alpha 12 FL (Q231L)	this paper	N/A
GFP-G protein-alpha 12 WT	this paper	N/A
GFP-G protein-alpha 12 delta-E cadherin	this paper	N/A
Porcine GFP-myosin VI	Gift from Dr. T. Hasson, University of California, San Diego, USA	Hasson and Mooseker (1994). PMID:7929586
Porcine GFP-myosin VI L310G	this paper	N/A
Alpha Catenin Tension Sensor	Constructed and validated in this lab	Acharya et al. (2017). PMID: 28329679
Software and Algorithms		
MATLAB	MathWorks	RRID:SCR_001622
Fiji	ImageJ, NIH	RRID:SCR_002285
GraphPad prism	GraphPad	RRID:SCR_002798

CONTACT FOR REAGENT AND RESOURCE SHARING

Further information and requests for resources and reagents should be directed to and will be fulfilled by the Lead Contact, Alpha S. Yap (a.yap@uq.edu.au).

EXPERIMENTAL MODEL AND SUBJECT DETAILS

Male human colorectal Caco-2 cells were cultured in RPMI media supplemented with 10% FBS, 1% non-essential amino acids, 1% l-glutamine and 1% penicillin/ streptomycin. Cells were tested for mycoplasma and source cultures maintained in low doses of plasmocin (Invivogen) to prevent mycoplasma contamination. E-Cad-GFP Caco-2 cells generated by CRISPR/Cas9 genome editing were described earlier (Liang et al., 2017).

METHOD DETAILS

Application of Equibiaxial Static Stretch

Caco-2 monolayers was grown on collagen-coated 25 mm BioFlex culture plates. Cells were subjected to static stretch using a Flexcell Fx-5000TM Tension System (Flexcell International, Hillsborough, NC) for 10 min with 10% strain. Control wells were plugged at

the bottom by rubber capping without application of any stretch. The inhibitors were present during the static stretch wherever needed.

Transfection and Reagent Use

Target proteins were depleted by RNAi in Caco 2 cells using custom designed or commercially available siRNAs (Invitrogen, Sigma USA or IDT, Singapore). Cells were transfected at 50-60% confluency using Lipofectamine 3000 (Invitrogen) for expression constructs or RNAiMAX (Invitrogen) for RNAi oligonucleotides according to the manufacturer's instructions. Cells were processed for experiment and analysis 24-48 h post transfection as required. Relevant siRNA sequences are shown in Table S2. Algorithms from Dharmacon were used to generate RNAi sequences for custom designed siRNA targeting the ORF or the 3'UTR.

Primary antibodies used in this study were: rabbit pAb against Phospho-myosin light chain 2 (1:200 IF, 1:1000 WB), mouse mAb against Myosin light chain 2 (1:1000 WB), rabbit pAb against α-Catenin (1:100 IF, 1:1000 WB); rat pAb α-18 (1:200 IF), goat pAb against p114RhoGEF (1:50 IF, 1:250 WB), rabbit pAb against p114RhoGEF (1:100 IF, 1:1000 WB), rabbit pAb against Gα12 (1:100 IF) rabbit pAb against Gα12 (1:100 IF, 1:500 WB), rabbit mAb against Gα13 (1:100 IF, 1:500 WB), rabbit pAb against GEFH1 (1:100 IF, 1:1000 WB), mouse mAb against LARG (1:100 IF, 1:1000 WB), rabbit pAb against ECT2 (1:50 for IF, 1:500 WB), rabbit mAb against p115RhoGEF (1:25 for IF, 1:200 WB), mouse mAb against E-cadherin (clone HECD-1, 1:1000 WB); rat mAb against E-cadherin (1:500 IF), mouse mAb against Myosin IIA (1:250 IF); rabbit pAb against Myosin IIA (WB only, 1:2500); rabbit pAb against Myosin IIA (1:100 IF); mouse mAb against Myosin IIB (1:100 IF); rabbit pAb against Myosin IIB (WB only, 1:2500), Myosin IIB (1:100 IF), rabbit pAb against Myosin VI (for IF only 1:200); mouse mAb against Myosin VI (WB only, 1:250), mouse mAb against GFP (1:500 IF, 1:5000 WB), Phalloidin conjugated with AlexaFluor546 or AlexaFluor647 (Thermo Fisher Scientific; 1:250) was used to label F-actin.

The species-specific secondary antibodies used for immunofluorescence in this study were conjugated with AlexaFluor 488, 546, 594 and 647 (Thermo Fisher Scientific, 1:500) or with horseradish peroxidase conjugated secondary antibodies (Bio-Rad Laboratories, 1: 5,000/10,000) for immunoblotting.

Cells were treated with Calyculin A (20 nM, 12-30 min) or Y-27632 (30 μM, 1 h). For RhoA activity inhibition, cells were treated with 1 μg/ μl of cell-permeable RhoA inhibitor (C3 Transferase) for 1h before Calyculin A addition. GPCR inhibitors used for these study were: JTE-013, CYM50358, W146 Hydrate, H2L5186303, Ki-16425, FR-171113 and ML354. Cells were incubated with these inhibitors (final concentration 0.1-0.3 μM respectively for 1h) before the experiments performed.

Plasmids

The CFP-p114RhoGEF construct was used as a template for generating p114RhoGEF-Y260A mutant by using the Quick Change V Site Directed Mutagenesis Kit (New England Biolabs, USA) as per the manufacturer's protocol and the corresponding primers are listed in Key Resource Table. Untagged G protein-alpha 12 (Q231L) construct was used as template to PCR amplify the full-length protein and was subsequently cloned into pEGFP-C1 (Clontech) using EcoR1 and BamH1 restriction sites. For Gα12ΔEcad construct, we PCR amplified fragment-1 (1-130 aa) and fragment 2 (197-365 aa) and were subsequently cloned in to pEGFP-C1 (Clontech) using EcoR1/Knp1(fragment 1) and Knp1/BamH1 restriction sites. Porcine GFP-myosin VI construct was used as the template for generating GFP-myosin VI L310G mutant with the the Quick Change V Site Directed Mutagenesis Kit (New England Biolabs, USA) as per the manufacturer's protocol; relevant primers are listed in Key Resource Table. For GFP myosin VI-ΔC construct, a PCR amplified fragment (1-1020 aa) from full-length GFP myosin VI was subsequently cloned into pEGFP-C1 (Clontech) using EcoR1 and BamH1 restriction sites. The details of construction and validation of the αCat-TS construct are described elsewhere (Acharya et al., 2017).

Immunofluorescence and Live-Cell Microscopy

For immunofluorescence, cells were either fixed with methanol at −20°C or with 4% paraformaldehyde in cytoskeleton stabilization buffer (10 mM PIPES at pH 6.8, 100 mM KCl, 300 mM sucrose, 2 mM EGTA and 2 mM $MgCl_2$) and subsequently permeabilized with 0.25% Triton-X in PBS. Upright Zeiss LSM 710 Meta scanning microscopes (63X, 1.4NA Plan Apo objective) driven by Zen software (ZEN, 2012, Zeiss) were used for fixed imaging. Zeiss ELYRA PS.1 SIM/STORM microscope (63X, 1.4NA Plan Apo objective) with sCMOS camera driven by Zen software (ZEN, 2012, Zeiss) was used for SIM imaging. All image reconstruction and channel alignment were performed within the ZEN software.

For live cell imaging, FRAP and FRET experiments, the cells were grown in 29 mm diameter borosilicate glass-bottomed dishes (Shengyou Biotechnology) and imaged in movie medium (15 mM HEPES, pH 7.5; 5 mM CaCl2; 10 mM D-glucose; 2.5% FBS in Hank's balance salt solution) at 37°C. E cadherin-GFP movies and FRAP were conducted on Inverted Zeiss LSM 710 Metal NLO AiryScan confocal system. For FRAP, either a 488 laser or Mai-Tai-eHP multiphoton laser (2000mW laser power) with dedicated BiG(GaAsP) detectors used. FRET analysis was conducted using LSM 710 Meta confocal with BiG (GaAsP) detectors for CFP/YFP imaging.

Proximity Ligation Assay (PLA)

For *in situ* protein-protein interaction analysis we have used the proximity ligation assay (Duolink® In Situ PLA detection reagents, Mouse/Rabbit, Sigma-Aldrich) using the manufacturer's protocol and our validated antibodies. For IF based PLA analysis, we masked the junction using the F-actin staining and measured the PLA dots on that masked region for all images using ComDet plugin

of ImageJ. To analyse the fluorescence intensity at vertices, a constant circular ROI of 3.1 μm diameter was drawn encircling the vertices. The mean intensity of all pixels within that ROI was calculated and plotted for E-cadherin and F-actin in different experimental conditions.

FRET and FRAP Analysis

For αE-Cat TS FRET (Acharya et al., 2017), human αE-Catenin specific siRNA transfected Caco-2 cells were reconstituted with αE-Cat TS by transient transfection and processed for FRET experiments after 24 h. Cells were imaged live (Calyculin A) at 37°C or in fixed material (Stretched membrane) by confocal microscopy. Images were acquired by sequential line acquisition. Donor (mTFP1 in CFP channel) and FRET channels were recorded by scanning using a 458nm laser; the emission was collected in the donor emission region (BP 460–490 nm) and acceptor emission region (BP 520–560 nm), respectively. The acceptor (VenusA206K in YFP channel) was imaged using a 514 nm laser line for excitation and emission was collected in the acceptor emission range (BP 530–560 nm). FRET index was calculated pixel by pixel as the ratio between the FRET channels and acceptor channel. Data showing the normalized FRET index compare to untreated control. For RhoA-FRET, Caco-2 cells were transfected with control or respective siRNA 24 h before the transfection of pTriEx-RhoA biosensor. FRET measurements and analysis were performed 36 h after biosensor transfection following mechanical stretch (fixed cell) or calyculin A treatment (live at 37°C). The Donor (CFP) and FRET channels were excited using the 458 nm laser line and emissions were recorded between 470 and 490 nm (Donor) and between 530 and 590 nm (Acceptor, YFP), respectively. The Acceptor channel was excited using the 514 nm laser line and the emission was recorded between 530 and 590 nm. The average FRET/YFP emission ratios were calculated as FRET index on a pixel-by-pixel basis at the apical junctions. Only pixels in the linear range within the ROIs of both the YFP and CFP channels were included them in FRET calculation as described earlier (Ratheesh et al., 2012). Briefly, mean FRET/YFP ratio of junctional pixels of three independent experiments were normalized with untreated or unstretched control and plotted for statistical analysis. We determined the linear pixels in our images by calculating the emission ratio of FRET/YFP and FRET/CFP for every pixel present within the ROIs across all of the images of the control condition. We therefore sorted all pixels according to Acceptor and Donor intensity values. For each intensity value, an average FRET emission ratio was calculated using a custom-made MATLAB script. We plotted the average FRET emission ratios for FRET/YFP and FRET/CFP against Donor and Acceptor intensities, respectively. Non-linear behaviour was seen as an overflow of the FRET emission ratio (FRET/YFP or FRET/CFP), and an appropriate threshold of intensity values was determined to exclude the pixels within this non-linear region before further analysis.

For FRAP analysis Caco-2 cells were first transfected with siRNA targeted against either the UTR region of p114RhoGEF, Gα12 or ORF of Myosin VI. After 24 h, the respective KD cells were transfected with GFP-p114RhoGEF, GFP-Gα12 and GFP-Myosin VI WT or L310G. For E-cadherin FRAP we used the CRISPR/Cas9-engineered E-cadherin-GFP line. To obtain FRAP profiles, a constant circular ROI was drawn in the centre of the junction (orto encircle the vertices) and was bleached to 70–80% with 810 nm laser (for p114RhoGEF, Gα12 and Myosin VI; at 26%, 1 iteration). For E-cadherin, 488 nm laser at 100% transmission was used for photobleaching. Time-lapse images were acquired before (pre-bleach) and after bleaching with a constant interval. The average fluorescence intensity F(Tt) over time in bleached area was analysed with ImageJ. The mean values of all frames before bleaching was used as the pre-bleached value F(Tp). The value of the first frame after bleaching was defined as F(To). FRAP values were the calculated as:

$$FRAP = \frac{F(Tt) - F(To)}{F(Tp) - F(To)} = Mf\left(1 - e^{\ln 2 \cdot t/t\frac{1}{2}}\right),$$

the calculated recovery fluorescence was plotted over time, where Mf is the mobile fraction, $t_{1/2}$ is the half time of recovery and Tt is time in seconds. The FRAP values were fitted using a nonlinear regression and the exponential one or two-phase association model (only for junctional p114RhoGEF) using Y0 = 0 and where Mf corresponds to the plateau value in Prism software. The immobile fraction was then calculated as:

$$Immobile\ fraction = 1 - Mf = 1 - \frac{F\infty - F(To)}{F(Tp) - F(To)}.$$

Mean ratios of independent experiments were plotted and used for statistical analysis.

Junctional Tension Measured by Recoil after Laser Ablation

We used a 2-photon laser ablation technique to assess tension at E-cadherin-GFP junctions, as described in detail earlier (Michael et al., 2016). Briefly, experiments were done at 37°C on a Zeiss LSM710 system (63x, 1.4NA Plan Apo objective) using 26% transmission of the 810nm laser and 10 iterations. MTrackJ plugin in Fiji software was used to analyse the strain or deformation of the cell-cell junction as a function of time after ablation. A mono-exponential growth curve fitted the change in junctional strain over time (saturates within the experimental time scale) which was modelled as a Kelvin-Voigt fiber. We therefore calculated the initial recoil (the rate of recoil at t=0) for each junction ablated. The average initial recoil value for the total number of junctions (for each experiment) was compared over three independent experiments. From Kelvin-Voigt fiber model, we assume that for different experimental conditions there is a variability in tensile force present on junctions (estimated by comparing initial recoil values between different conditions) but the viscosity is not significantly different between them. We tested the validity of our assumption that for different experimental conditions, there is a variability in tensile force present on junctions (compared by initial recoil values between

conditions) but not the viscosity significantly, by measuring the rate constant *k* of strain growth after ablation (Michael et al., 2016), amongst different conditions. No significant differences were noticed in *k*-value, as would be expected to occur if changes in either viscosity or elasticity of the junctions were significant.

Traction Force Microscopy (TFM) and Analysis of Internal Cellular Stress

For traction force measurements, cover glasses were spin-coated with polydimethylsiloxane (PDMS) bearing a Young's modulus of 15kPa, further functionalized with a solution of carboxylated nanobeads (diameter 200nm; Molecular Probes Thermo, Fisher) and then coated with a solution of fibronection (10 μg/ml). Cells grown on bead-coated substrate were imaged with a Nikon deconvolution scope equipped with temperature and CO_2 regulated incubator. DIC and Far-red (nanobeads) images were taken at 0 min and 8 min after adding CalyA or DMSO control (0.2% v/v). At the end of the movie, cells were removed by trypsinization to obtain the null-force positions of the beads. The compiled stack of images was mapped via PIV (Particle Image Velocimetry) analysis to assess the displacement field of the beads. The window size was set to 16 pixels. Subsequently, the traction force data were analysed with Bayesian Inversion Stress Microscopy (BISM) for internal stress field of a cell monolayer, as described previously (Nier et al., 2016).

Nematic Order Analysis of F-Actin

F-actin alignment at vertices was analysed in SIM images of phallodin-stained samples by the nematic order parameter tensor Q using the method of Reymann et al. (2016). Given the high filament density at junctions, this approach analyses average orientation at the micron-scale. To create a director field, an entire vertex region was cropped as a 7.5 μm x 7.5 μm square, oriented so that a bicellular junction bisected the vertex in the image field, and segmented randomly into small, overlapping 1.5 μm x 1.5 μm square (N= 24 pixels) windows. The local F-actin orientation (director) was calculated for each window by transforming the pixel intensity of that image domain into Fourier space. For Q tensor orientation in the image domain, the nematic director was oriented parallel to the bicellular junction that bisected the vertex in the image field.

Immunoprecipitation and Immunoblotting

For Gα12 and Myosin VI GFP-trap experiments, Caco-2 cells were cultured on 10 cm culture dishes, at 50-60%% confluence for transfection with siRNA (wherever necessary) using lipofectamine RNAiMax; after 24 h the GFP tagged expression constructs (~20 μg) were transfected with Lipofectamine 3000 (Invitrogen). The clarified cell lysate was incubated with GFP-trap beads. Following incubation, GFP-trap beads were washed several times in lysis buffer supplemented with 300 mM NaCl. The protein complexes were then resolved by SDS-PAGE and immunoblotted. For immunoprecipitation of endogenous E-cadherin, 1mg of total protein was added to 200 μl of culture supernatant of E-cadherin monoclonal antibody. Following overnight rotation, the lysate-antibody solution was incubated with a packed slurry of Protein A. Protein A Beads were then washed three times on ice to remove non-specific binding, boiled in the SDS-PAGE loading buffer and then centrifuged at 12,500 g; 10 min. The supernatants were subjected to Western blotting.

Transepithelial Electrical Resistance (TEER) Measurements

$2x10^5$ Caco 2 cells were plated and grown to confluence on Transwells with polyester membrane inserts (12 mm diameter, 0.4 mm-pore size; Corning, MA). TEER was measured using a Millicell-ERS epithelial volt-ohmmeter (Millipore, Billerica, MA). TEER values (ohms.cm2) were normalized based on the area of the monolayer and was calculated by subtracting the blank values from the filter and the bathing medium. For C3T treatment, the cells were pre-incubated for 45 min. with C3T and then DMSO or calyculin was added for 15 minutes and TEER was measured for indicated time points after 21 days culture the cells. For p114 RhoGEF KD, cells were transfected on day 18. siRNAs were mixed with Opti-MEM and RNAiMAX, added to the apical and basal and incubated for 6 h, before being replaced with fresh RPMI without antibiotics. TEER measurements were performed on day 21. DMSO or calyculin were added for 15 min before measurement of TEER.

QUANTIFICATION AND STATISTICAL ANALYSIS

Image Processing and Analysis

Quantitative analysis of junctional intensity of E-cadherin, NMIIA, NMIIB, F-actin, αE-Catenin and α18 was performed in ImageJ software (NIH) with the line scan functions by drawing a line of 12 μm in length (10-pixel wide) orthogonal to, and centred on, randomly selected homotypic junctions. Optical Z-stacks (0.2 μm intervals) were acquired to correct for cell heights and to focus on all junctions analyzed. The pixel intensities along the selected line were recorded and plotted, the fluorescence profiles were fitted to a Gaussian curve and the peak values (fluorescence intensities at junctions) were obtained from this fitting. The average pixel intensity values lying on either side of the center (at junctions) on the masking line were considered as background fluorescence and subtracted from the plots. To correct for fluctuations in the height of cells within frames, some representative confocal images (identified in figure captions) are presented as maximum projection views of the three most-apical sections of the cells (0.19 μm intervals between the sections). The junctional intensity of α18 is presented as the ratio of junctional α18 and junctional αE-Catenin. To quantify GFP-AHPH, Gα12 and different RhoA GEFs we measured the ratio of junctional intensity and cytoplasmic **mean fluorescence** intensity in ImageJ. A 10-pixel wide line (using the freehand drawing tool) was drawn covering the whole region of a junction, and the mean pixel intensity of this region was measured as the junctional GFP-AHPH. For GEFs and Gα12, the masking was done on the corresponding

E-cadherin in the other channel of the same image. Mean cytoplasmic GFP-AHPH, GEFs and Gα12 fluorescence was measured by masking the entire cytoplasm of cells and calculating the average pixel intensities within that mask.

Data are presented as the ratio values normalized to the corresponding ratio value for control conditions and the normalized ratio of junctional versus cytoplasmic fluorescence intensity is referred to as Junctional AHPH, Junctional GEFs or Junctional Gα12.

To quantitate fracture initiation from movies, we measured the change in number of intact vertices (as fractures were overwhelmingly initiated at vertices). We measured the number of intact vertices present at each sample time point (using Tissue Analyzer and ComDet plugin of ImageJ), subtracted this from the total number of vertices present at the start of the movie, and normalized this difference value to the initial number of vertices. For junctional fracture index, the entire image was segmented into small square templates and the number of junctions were counted. The mathematical description of the Fracture Index is described in the Computational Supplement (Data S1, Equation 19).

For intensity LUT application in different images, all images are converted to 8-bit images and pixel intensity of whole image was to a minimum and maximum scale of 0-255. Therefore, the FIRE or Rainbow LUT was applied to the respective images and the intensity was equally adjusted for all conditions. Images were then locked for intensity alteration by adding calibration bar.

Statistical Analysis

All data displayed are represented as mean ± SEM, derived from three independent experiments as indicated in figure legends. For quantitation of fluorescence intensity from fixed material, 30-50 junctions were analysed for each individual experiment. For live-cell imaging experiments (FRET, AHPH and FRAP) 10-15 cells/experiment/condition were analysed.

All statistical analyses were performed using GraphPad Prism. Unpaired two-tailed t tests were used to compare datasets consisting of two groups, and a Welch's correction was included when data normalized to the control values were being assessed. One-way ANOVA with Dunnett's post hoc test was used to compare three or more groups. For comparing two different independent conditions with three or more groups two-way ANOVA with with Sidak's multiple comparisons test was performed.

DATA AND SOFTWARE AVAILABILITY

The MATLAB scripts for FRET analysis as the codes for simulations of the vertex model described in this paper are available on request.